TURUN
YLIOPISTO
Matemaattis-luonnontieteellinen
tiedekunta

Structural geological 3D-model combining geophysical surface measurements and borehole data at the Kopparnäs site, S Finland

Miikka Muurinen

Bedrock geology
Master's thesis

29.1.2026
Turku

Master's thesis

Subject: Bedrock Geology
Author: Miikka Muurinen
Title: Structural geological 3D-model combining geophysical surface measurements and borehole data at the Kopparnäs site, S Finland
Supervisor: Dr. Eemi Ruuska, Dr. Jon Engström
Number of pages: 59 pages
Date: 29.1.2026

The study of faults and fracture systems within crystalline bedrock has become a major point of interest in recent years. Traditional methods such as field mapping and remote sensing have certain limitations regarding for example assessment of horizontally oriented structures and survey depth penetrations. Therefore, alternative methods are needed to assess horizontal fracturing and their three-dimensional attributes. The purpose of this study is to model fracturing at the Kopparnäs study site in southern Finland with the focus on the horizontal fracturing and the geometrical attributes of fracturing, such as sizes, orientations, intensity and variance in depth. The study acts as groundwork for further investigations regarding for example DFN- and fluid flow modelling.

In this work, a joint use of surface gathered- and subsurface geophysical data was employed. The surface gathered data consists of a set of structural field measurements, 6 ERT survey lines and 9 GPR survey lines. The borehole R307 was used for collecting subsurface information which included OBI/ABI images, numerical fracture data derived from OBI/ABI images and a BHGPR image conducted from the borehole. In addition, open-source aeromagnetic maps and digital elevation models were used.

Fracture traces from crosscutting and parallel running GPR survey lines were linked to form three dimensional horizontal to subhorizontal planes representing fracture surfaces. In total 47 horizontal fracture planes were created in 7 clusters. Field measurements near the clusters were extruded to planes representing upright fracturing. In addition, three major fault planes were identified and modelled. Numerical fracture data from borehole R307 was linked with fracture traces based on the BHGPR image to produce a fracture set with determined fracture geometries in depth.

The joint methods in this study proved adequate for i) modelling approximations of fault plane geometries ii) identifying and imaging horizontal fractures in homogenous surface layer bedrock, iii) 3D modelling horizontal fracture surfaces with quantified geometries, iv) imaging strongly reflecting discrete fractures and fracture zones in depth and v) determining the geometries of these fractures and modelling them as 3D surface. This thesis provides a workflow for incorporating often excluded hydraulically conductive horizontal fractures into structural 3D models and a method for increasing depth penetration of fracture network analysis. These results can be used to increase the accuracy of deterministic 3D fracture system characterization in the future.

Key words: bedrock structures, fracture network, ground penetrating radar, borehole radar, geological 3D model, subhorizontal fractures

Pro gradu -tutkielma

Pääaine: Kallioperägeologia
Tekijä: Miikka Muurinen
Otsikko: Structural geological 3D-model combining geophysical surface measurements and borehole data at the Kopparnäs site, S Finland
Ohjaajat: Eemi Ruuska, Jon Engström
Sivumäärä: 59 sivua
Päivämäärä: 29.1.2026

Kiteisen kallioperän siirrosten ja rakosysteemien tutkiminen on muodostunut tärkeäksi kysymykseksi viime vuosien aikana. Perinteisillä kenttä- ja kaukokartoitusmenetelmillä on tietyt rajoitteet liittyen esimerkiksi vaaka-asentoisten rakenteiden tutkimiseen ja tutkimusten syvyystarkkuuteen. Kun halutaan tutkia vaaka-asentoisia rakenteita ja niiden kolmiulotteisia ominaisuuksia, on käytettävä vaihtoehtoisia metodeja. Tämän tutkimuksen tavoite on mallintaa rakoilua Kopparnäsin tutkimusalueella eteläisessä suomessa. Tutkimuksessa keskitytään vaaka-asentoisiin rakoihin ja niiden geometrisiin ominaisuuksiin, kuten koko-, suunta-, intensiteetti- ja syvyysjakaumaan. Tutkimuksen tuloksia on tarkoitus käyttää esimerkiksi DFN- ja fluidien virtauksen mallinnukseen tulevaisuudessa.

Työssä on käytetty maan pinnalta ja maan alta kerättyä geofysikaalista aineistoa. Pinta-aineistoon kuuluu kentällä tehtyjä rakomittauksia, kuusi ERT-mittauslinjaa ja yhdeksän GPR-mittauslinjaa. Kairareiästä R307 kerätty maanalainen aineisto sisältää OBI/ABI kuvat, edellä mainituista johdettu numeerinen rakodata ja reiästä otettu BHGPR kuva. Lisäksi apuna on käytetty avoimena saatavilla olevaa aineistoa, kuten aeromagneettista karttaa ja digitaalista korkeusmallia.

Leikkaavien ja vierekkäisien GPR linjojen rakoviivatulkintoja linkitettiin yhteen ja niistä muodostettiin tasoja, jotka edustavat vaaka-asentoisia rakopintoja. Tuloksena oli kaikkiaan 47 rakopintaa, jotka ovat jaettuna seitsemään eri alueelliseen ryhmään. Näiden ryhmien alueella sijaitsevat kenttämittaukset tursutettiin pinnoiksi edustamaan pystyasentoista rakoilua. Lisäksi kolme suurempaa siirrospintaa havaittiin ja mallinnettiin. Numeerinen rakodata R307 kairareiästä linkitettiin BHGPR kuvan kanssa, minkä avulla kairareiästä saatiin tulkittua rakosetin geometriset ominaisuudet.

Tutkimuksessa käytettyjen menetelmien avulla pystyttiin i) mallintamaan arvioita siirrospintojen geometrioista, ii) havaitsemaan ja mallintamaan vaakatasoisia rakoja homogeenisen kallioperän pintakerroksissa, iii) mallintamaan rakopintoja ja määrittämään niiden geometrisia ominaisuuksia, iv) kuvantamaan voimakkaasti heijastavia rakoja ja rakovyöhykkeitä syvällä ja iv) määrittämään näiden rakojen geometriset ominaisuudet ja mallintamaan ne pintoina. Tämä työ esittelee tavan, jolla voidaan lisätä rakennegeologisiin 3D-malleihin usein pois jätetyt vettä johtavat vaakaraot ja menetelmän, jolla voidaan lisätä rakosysteemien tutkimisen syvyystarkkuutta. Näitä tuloksia voidaan käyttää tulevaisuudessa determinististen 3D-rakomallien tarkkuuden parantamisessa.

Avainsanat: kallioperän rakenteet, rakoverkko, maatutka, kairareikätutka, geologinen 3D malli, vaakaraot

Contents

1 Introduction

The study of fluid flow in crystalline rock has become important in the fields of nuclear waste disposal and geoenergy (Hartley et al., 2018; Bossennec et al., 2021; Chabani et al., 2021; Frey et al. 2022; Piipponen et al. 2022). The ability of fluid to flow through a matter is known as permeability. In low permeability environments such as the crystalline bedrock of Finland, fluid flow is largely controlled by fractures and their properties such as orientation, size, curvature, density, aperture as well as connectivity of individual fractures and fracture sets (Leckenby et al., 2005; Sanderson and Nixon, 2015; Escallon et al., 2024). In crystalline rock, these networks are usually associated with faulting (Caine et al., 1996; Davy et al., 2006; Faulkner et al., 2010). The traditional fault zone anatomy by Caine et al. (1996) includes the main slip surface/volume, or "fault core", and the secondary fractures of the surrounding damage zone. In this model, the fault core is considered as a flow barrier, due to the impermeable nature of fault gouge and the damage zone as an along fault conduit due to developed fracture network. Faulkner et al. (2010) have since presented varying architectures of fault zones that describe the possibility of large anisotropies of permeability within individual fault zones. This in turn highlights the importance of detailed assessment of different fracture networks.

Commonly used methods of fracture network characterization include remote sensing of faults and fractures as well as field mapping (Lei et al., 2017; Romano et al., 2020; Bossennec et al., 2021; Frey et al., 2021; Smeraglia et al., 2021; Engström et al., 2025) Remote sensing works well in preserving the geometrical features of fractures such as curvature, segmentation and complex topological relationships, whereas detailed field mapping can be utilized to assess other important attributes such as dip distributions and fracture apertures (Leckenby et al., 2005; Lei et al., 2017).To improve assessments of 3D properties, non-outcropping subhorizontal fractures, and enhanced depth penetration, additional methods must be employed. These include ground-penetrating radar (GPR), optical and acoustic borehole imaging (OBI/ABI), and borehole ground-penetrating radar (BHGPR). GPR can be utilized from the surface to image gently dipping structures (Meschede et al., 1997; Porsani et al., 2006; Markovaara-Koivisto et al., 2014; Walton et al., 2015; Molron et al., 2020; Tao et al., 2022; Song et al., 2025) whereas BHGPR is used to image properties of often steeper dipping fractures at greater depths (Olsson et al., ,1992; Serzu et al., 2004; Dorn et al., 2012; Escallon et al., 2024). GPR methods have

been used when determining individual fractures and their properties (e.g., Tsoflias and Hoch, 2006; Markovaara-Koivisto et al., 2014; Escallon et al., 2024) as well as larger fault zones and systems consisting of multiple fractures (Meschede et al., 1997; Serzu et al., 2004; Christie et al., 2009; Dorn et al., 2013; Song et al., 2025)

In this study, I use surface-gathered and borehole GPR images, along with supporting data, to model faults and fault proximal fracturing in 3D at the Kopparnäs study site, Inkoo. The aim of the study is to produce a 3D geological model which contains structural features and statistical data (such as orientations, spatial extents, and intensity) on faults, and fractures in the area. Focus is placed on horizontal to subhorizontal fracturing and their variance depending on their regional location and occurrence in depth. The purpose of the 3D model is to guide further developments, such as the discrete fracture network (DFN) and fluid flow modelling in the area. The thesis is conducted in cooperation with the University of Turku and the Geological Survey of Finland (GTK).

2 Geological Background

2.1 Svecofennian orogeny and post collisional tectonics

The bedrock of Southern Finland was formed in the Svecofennian orogeny around 1.95-1.75 Ga, in the amalgamation of multiple island arcs and microcontinents into the Archean craton (Korja et al., 1993; Nironen, 1997; Kähkönen, 2005; Lahtinen et al., 2005; Vaasjoki et al., 2005). This modern model of accretionary terrains differs from the traditional model of continuous subduction (Gorbatschev and Bogdanova, 1993). The three main amalgamated crustal blocks that formed the Svecofennian units of Finland are Savo belt, Keitele microcontinent and Tavastia island arc (Lahtinen et al., 2005). The Svecofennian province in Finland can be divided into the Southern Finland Subprovince (SFS) and Western Finland Subprovince (WFS, fig. 1).

Fig. 1. Provinces of the Fennoscandian shield (modified from Nironen, 2017)

In Lahtinen et al. (2005) the complex evolution of the Svecofennian orogeny is subdivided into multiple orogenies. A simplified summary of island arc and microcontinent accretion in Finland is presented below.

In the Lapland-Savo orogeny, the already combined Savo belt and Keitele microcontinent collided into the Karelian Province from the west at 1.91-1.89 Ga, creating the core of the WFS (Lahtinen, 1994; Väisänen, 2002; Lahtinen et al., 2005). The SFS formed during the Fennian orogeny, where the Tavastia island arc collided from the south with the Keitele microcontinent at around 1.89-1.88 Ga (Väisänen et al., 2002, Lahtinen et al., 2005). The Svecofennian orogeny continued with the collision of Sarmatia into the formed continent from the SE at 1.84 Ga, known as the Svecobaltic orogeny. This was followed and partly overlapped by the Nordic orogeny at 1.82-1.79 Ga, where the Amazonian microcontinent collided into the NW parts of the Fennoscandia. The formed Paleoproterozoic supercontinent was formed and stabilized by the subsequent collapse of the orogeny at 1.79 Ga onwards (Lahtinen et al., 2005, fig. 2).

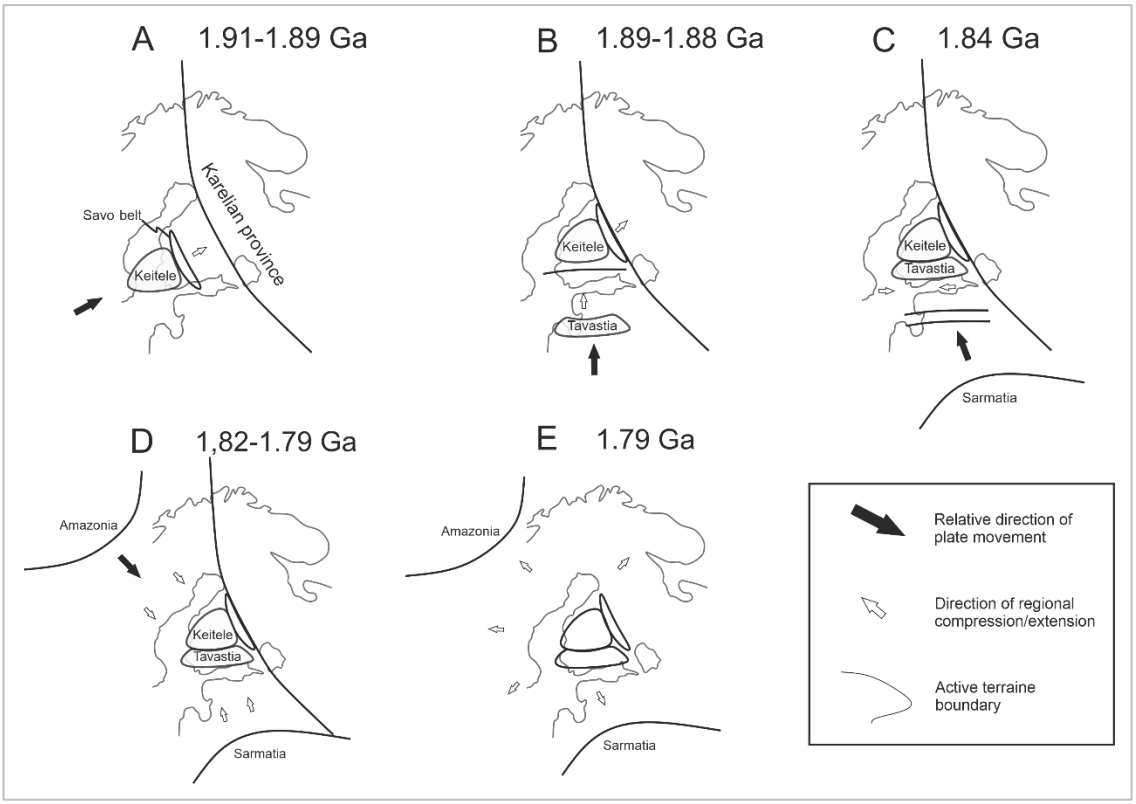

Fig 2. A simplified model of formation of the Svecofennian provinces of Finland after Lahtinen et al. (2005). A: Lapland-Savo orogeny, combined Savo belt and Keitele microcontinent collide into the Karelian Province from the west. B: Fennian orogeny, Tavastia island arc collides into the Keitele microcontinent from the south. C: Svecobaltic orogeny, the collision of Sarmatia into the formed craton from the south-east. D: Nordic orogeny, collision of Amazonia from the NW, partly overlapping with the Svecobaltic orogeny. E: Subsequent exhumation and collapse of the Svecofennian orogeny.

The deformation in the Svecofennian provinces of Finland has been divided into four deformation phases D1-D4. D2-D4 is mainly observed in areas of the SFS, since the ductile deformation in the WFS ceased almost immediately after 1.89-1.88 Ga (Väisänen, 2002). According to Väisänen (2002) the collision of Tavastia into Keitele formed the D1/D2 structures in 1.88-1.86 Ga. These structures are characterized by bedding parallel S_1 foliation, tight to isoclinical D2 folding and penetrative subhorizontal S_2 axial plane foliation. The S_1 has largely been overwritten by the subsequent deformation events (Stålfors and Ehlers, 2006).

The regional deformation phase D3 occurred at 1.83-1.82 Ga by which time several major shear zones are considered to have been formed in southern Finland (Torvela et al., 2008). D3 is roughly concurrent with the proposed collision with Sarmatia at 1.84 Ga (Elming and Mattsson, 2001; Lahtinen et al., 2005), and the deformation stage was defined in Väisänen (2002) as post-colliosional convergence. This oblique compression resulted in

NW-directed thrusting that was partitioned into domains of folding and shearing in the late stage of collision in Southern Finland (Korsman et al., 1999; Väisänen and Hölttä, 1999; Skyttä et al., 2006). During D3, pre-existing structures were being transposed into NE-SW to E-W trending upright or NW overturned folding (D3-folding, Torvela and Kurhila, 2022). Fold limbs were strongly migmatized, deformed and intruded by garnet-cordierite rich granites. Granites were also intruded as veins and dykes along S_3 axial planes. Age data from the leucosomes provide the age of D3 (1.82 Ga), though the anatexis continued until around 1.81 Ga (Väisänen, 2002). Torvela et al. (2008) suggest that bulk of the folding and mineral lineations at the SW margin of the SFSZ developed during D3 (or circa 1.83 Ga). D4 retrograde deformation (Skyttä and Mänttäri, 2008) at circa 1.79 Ga marked the last ductile reactivation of the shear zones, in which the deformation was solely localized (Skyttä et al., 2006; Torvela et al., 2008).

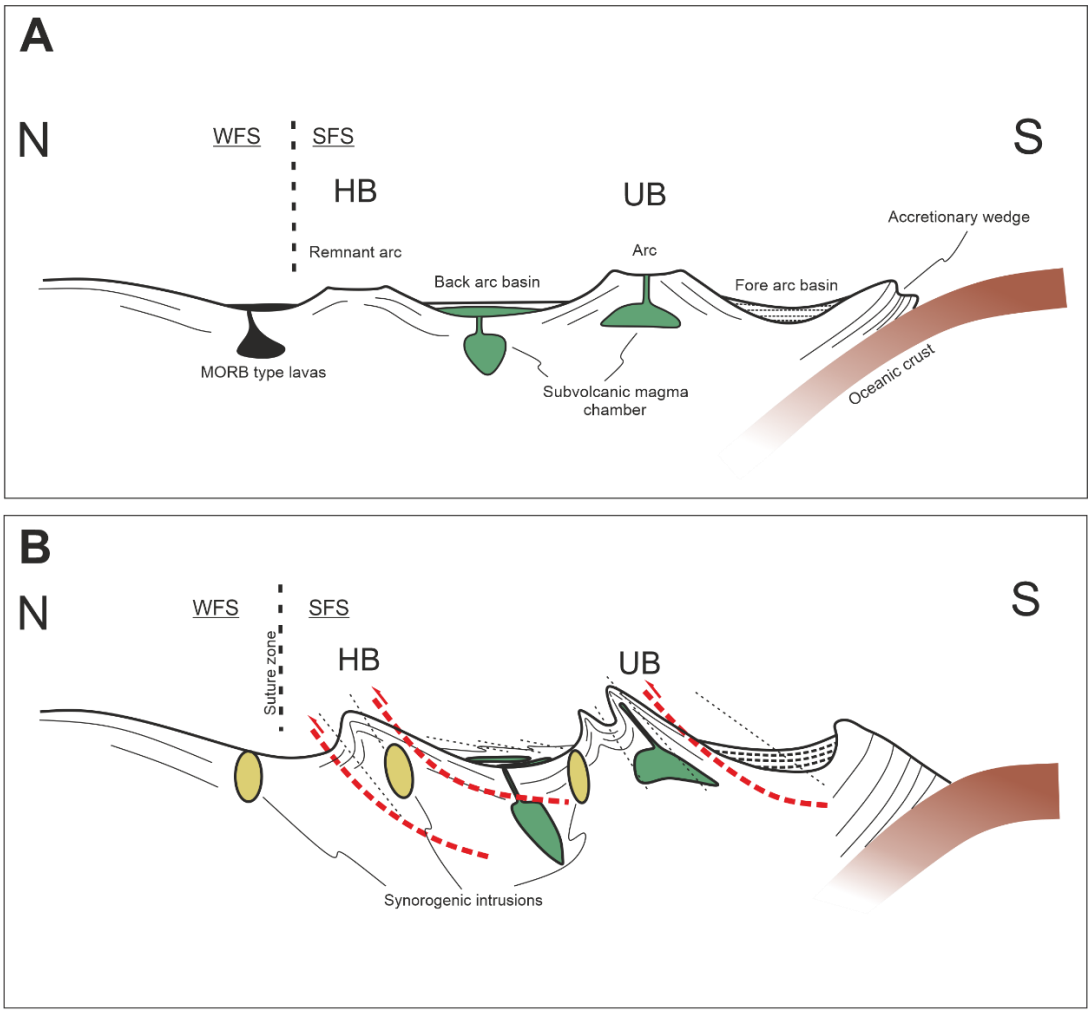

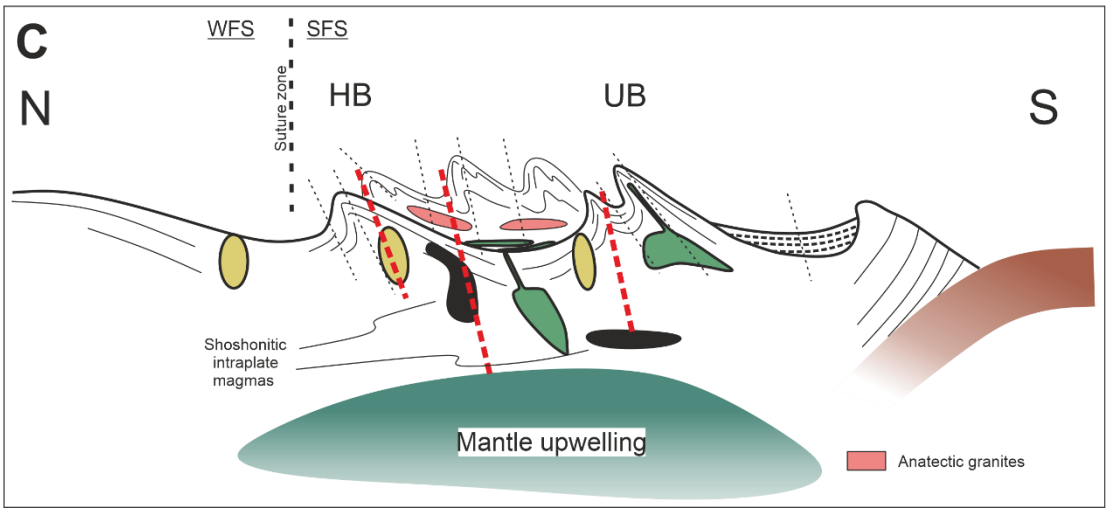

Fig. 3. Evolution of the SFS during the pre-collisional, collisional and post-collisional stages along a N-S profile (modified from Väisänen, 2002). A: Pre-collisional stage, HB=Häme belt, UB= Uusimaa belt (explained in chapter 2.2). B: Collisional stage (1.88-1.86 Ga) N-vergent structures. Dotted lines= S_2 foliations, dashed red lines=inferred thrusts. C: Post-collisional stage (1.86-1.80 Ga) continued deformation. Dotted lines=S_3 foliations, dashed red lines=late orogenic shear zones.

After D4, the rapid initiation of cooling and exhumation resulted in the onset of ductile-brittle transition at 1.79 Ga (Torvela et al., 2008). The first signs of brittle deformation in the vicinity of SFSZ are dated around 1.78 Ga (Torvela et al., 2008), whereas the first structures of brittle deformation were formed at around 1.75 Ga in Olkiluoto SW Finland (Mattila and Viola, 2014). Subsequent changes in the paleo-stress environment resulted in a series of brittle reactivations in the pre-existing shear zones and anisotropy created by previous (ductile) deformation across the Southern Finland (Heeremans and Wijbrans, 1999; Väisänen and Skyttä, 2007; Torvela et al., 2008; Mattila and Viola, 2014; Nordbäck et al., 2023) as well as the generation of new brittle deformation zones (Nordbäck, 2024). Using results from Olkiluoto Mattila and Viola (2014) concluded that in the brittle regime, Southwestern Finland has undergone multiple stages of brittle reactivations between 1.75 Ga and 0.9 Ga, beginning with a NW-SE to NNW-SSE transpression. From there the bedrock endured changing directions of transpression, extension, transtension and compression coinciding with the ongoing orogenic events on the edges of the Fennoscandian shield. The last stage is considered to be the E-W extension related to the collapse of the Sveconorwegian orogeny. By the end of the Mesoproterozoic (1.0 Ga), any continuation of brittle deformation would not generate new structures but reactivate pre-existing ones (Mattila and Viola, 2014). Though these studies are focused entirely on

the Olkiluoto area on the SW coast, it does highlight the complex evolution of the brittle stress regimes since the brittle-ductile transition.

The Fennoscandian shield has endured a multitude of glaciation events, with the latest having occurred from 115 ka to around 11 ka. Deglaciation at around 11 ka resulted in the isostatic rebound of the lithosphere, which is characterized by a vertical extension stress regime (Wu et al. 1999). The uplift commenced before the deglaciation was completed and reached its height (around 50 m in 100 years) just before the land was ice free. This isostatic uplift is responsible for the horizontally to subhorizontally oriented fracturing of the upper layers of the bedrock (Mörner, 1978).

2.2 Southern Finland Subprovince

The SFS tectonic province trends E-W and extends across southern Finland (Fig. 4). In the south, it terminates at the Gulf of Finland and in the north, it is bordered by WFS (Väisänen et al., 2002; fig. 4). SFS consists of Paleoproterozoic metavolcanic and metasedimentary (i.e., supracrustal) rocks, Paleoproterozoic intrusive suites, and later Paleo- and Mesoproterozoic rapakivi suites. The Paleoproterozoic intrusive rocks include the mafic layered intrusions, different plutonic suites, as well as the late Svecofennian granite-migmatite belt, and the rapakivi suites include most notably the Kymi rapakivi suite in southeastern Finland and the Åland rapakivi suite in southwestern Finland (Luukas et al., 2017). The SFS can be divided into two belts: the Häme belt and the Uusimaa belt, the latter of which is the host to the study area.

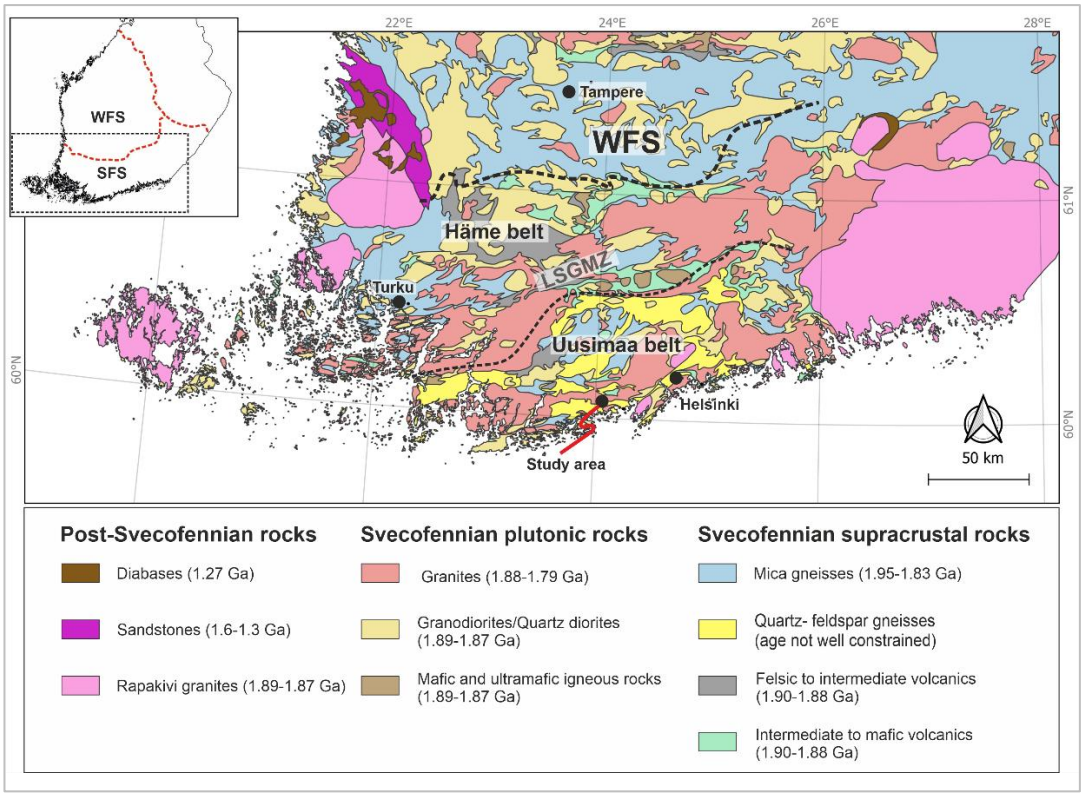

Fig. 4. Lithologies of Southern Finland. (Modified from Toivanen et al., 2025).

The Häme belt consists of intermediate to mafic volcanic rocks and metasedimentary rocks that are intruded by younger gabbros, diorites, granodiorites, and tonalites as well as late to post-tectonic granites, migmatites and pegmatites (Vaasjoki et al., 2005; references in Kara, 2021). The Häme belt formed at around 1.89-1.88 Ga and the supracrustal rocks have metamorphosed in mainly amphibolite facies between 1.88 – 1.85 Ga (Nironen, 1999; Väisänen, 2002; Hölttä and Heilimo, 2017). Later, a high-temperature event at 1.83 – 1.81 Ga formed the late Svecofennian Granite Migmatite Zone (LSGMZ) on the southern side of the Häme belt (Kähkönen, 2005).

The Uusimaa Belt consists of metasedimentary rocks, volcanic rocks from ultramafic to felsic composition and sedimentary carbonates. The volcanic rocks show continental margin and rifting type affinities (Kähkönen, 2005; Vaasjoki et al., 2005). The rocks have intruded as three groups: the 1.91 – 1.88 Ga synvolcanic rocks, 1.88 – 1.86 Ga synorogenic rocks and 1.84 – 1.81 Ga late- to postorogenic rocks (Huhma, 1986; Väisänen et al., 2000; Väisänen et al., 2002; references in Toivanen, 2023). However, the Uusimaa belt has indications of older, 2.1 – 1.91 Ga contributions (Kara et al., 2018). The western part of the belt hosts rocks of bimodal magmatism, and supracrustal rocks are

crosscut and migmatized by 1.88 Ga and 1.84-1.82 Ga granites (Vaasjoki et al., 2005). The sedimentary interlayered carbonate rocks are mostly associated with volcanic rocks and possibly some local chemical precipitants (Toivanen, 2023).

2.3 Shear zones of Southern Finland

As a result of strain partitioning during the regional deformation phases D2, D3 and D4, E-W and N-S striking large shear zones were initiated and subsequently reactivated in southern Finland (fig. 5). The E-W trending large shear zones (South Finland Shear Zone (SFSZ) and Somero Shear Zone (SSZ)) hosted the dextral movement of the westward drifting crustal block and the abutting N-S trending shears (such as Porkkala Mäntsälä Shear Zone (PMSZ), Jyly shear zone (JSZ) and the Kisko Shear Zone (KSZ)) hosted the internal thrust/dip-slip deformation of the mobile crustal block (Väisänen and Skyttä, 2007). In Torvela et al., (2008), U-Pb data suggests that the D2 deformation is closely concurrent with the 1.85 Ga earliest partitioning of stress into the South Finland Shear Zone (SFSZ), and possibly the other major shear zones. Out of the three shearing events/reactivations (D2-D4), the one concurrent with D3 was the strongest and was most likely responsible for the genesis of most of the shear zones (Väisänen et al., 2000; Torvela et al., 2008). The period of exhumation and orogenic collapse after ~1.79 Ga, resulted in an extensional environment that generated new E-side down normal faults (The Paimio Shear Zone (PMZ) and the Mynälahti Shear Zone (MSZ)) and reactivation of pre-existing structures (Heeremans and Wijbrans, 1999; Lahtinen et al., 2005; Väisänen and Skyttä, 2007; Torvela et al., 2008; Mattila and Viola, 2014). The study area is located near three larger shear zones: SFSZ, PMSZ and JSZ.

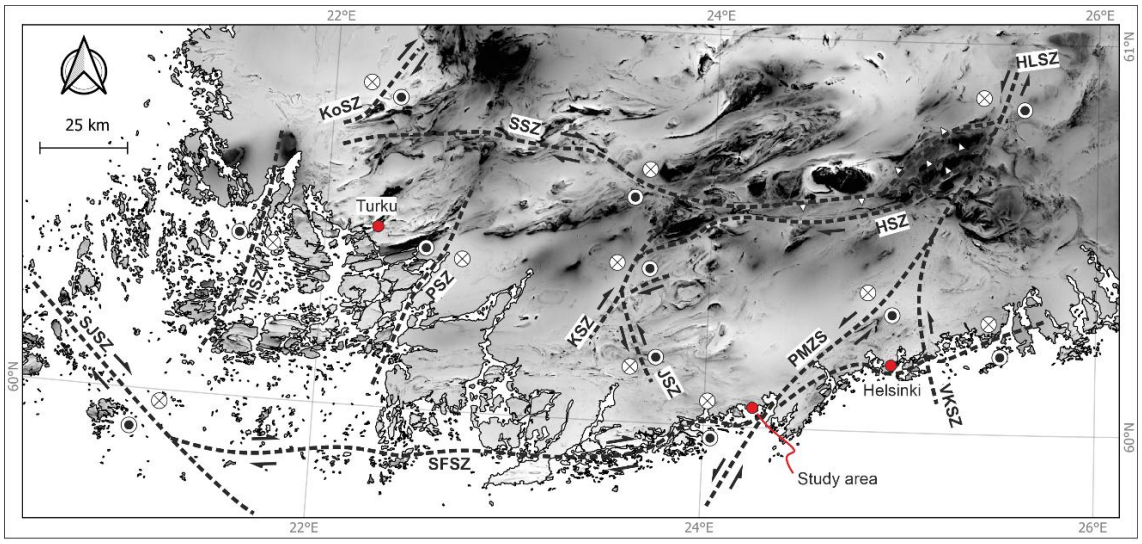

Fig. 5. The network of shear zones in Southern Finland. (Modified from Väisänen and Skyttä, 2006; Kauti, 2016).

SFSZ strikes E-W along the southern coast of Finland extending from the eastern side of Helsinki to the SW coast of Finland, where it connects to the Sottunga-Jurmo shear zone which can be observed around the islands of Turku archipelago (Torvela and Ehlers, 2010; fig. 5). The heavily deformed gneissic and mylonitic structures suggest that the shear plane is nearly vertical with a dextral strike-slip- and a south side up reverse component (Elminen et al., 2008). The dextral movement has been induced by NW-SE transpression and has been interpreted to be at least 20 km (Ehlers et al., 1993; Ehlers et al., 2004; Torvela and Ehlers, 2010). In addition to the periods of activity during D1-D4, SFSZ has reactivated at least once between 1.78 Ga – 1.58 Ga (Torvela et al., 2008). The subhorizontal slickenlines indicate that the brittle reactivation has been both dextral and sinistral (Pajunen et al., 2008).

PMSZ is a large shear zone running NE-SW through Southern Finland. It connects to the N-S oriented Vuosaari Korso shear zone in its NE end, and it continues through the SFSZ in its SW end, from where on it follows older ductile structures (Elminen et al., 2008). It also bends the structures of SFSZ towards NE (Pajunen et al., 2008). Pajunen et al. (2008) have interpreted the shearing to have initiated as sinistral strike-slip movement. This was then presumably followed by the E-side-up reverse movement and further followed by an episode of extensional brittle deformation due to the intrusion of rapakivi granites (Heeremans and Wijbrans, 1999; Elminen et al., 2006; Pajunen et al., 2008). These

rapakivi-induced late-stage brittle reactivations have been interpreted as dextral strike-slip faulting (Elminen et al., 2006; Pajunen et al., 2008).

Väisänen and Skyttä (2007) described the JSZ to be a network of four parallel mylonitic shear zones that form a positive flower structure some few kilometers wide. JSZ abuts the Kisko shear zone (KSZ) in the north and extends 35 km towards the southern coastline (fig. 5). The westernmost limb (referred in Väisänen and Skyttä, 2007 as JSZ I) is considered the main shear zone of the structure and between the mylonitic shears lie areas of folded domains. Kinematic indicators show that the shearing initiated in ductile, high temperature conditions in a sinistral manner, which was later transformed into the dominant E-side-up reverse shearing (Väisänen and Skyttä, 2007).

2.4 Kopparnäs

The study area of Kopparnäs is located in the municipality of Inkoo, within the Uusimaa belt. Laitala (1961) and Sakaguchi (2017) described the central parts of Inkoo as being dominated by quartz-feldspar gneisses, mica gneisses and amphibolites. These lithologies show compositional variations and complex ductile deformation structures, unlike the pegmatitic granites that are weakly foliated. These pegmatites host inclusions of supracrustal gneisses and synorogenic granitoids. Kopparnäs also hosts older E-W- and younger N-S trending diabase dikes. These dikes have intruded into structures formed in a SE-NW transpression which is also thought be a reactivation event in the E-W and N-S trending shear/fault zones (such as SFSZ and HSZ, Pajunen et al. 2008; Sakaguchi 2017). In the southeastern part, the bedrock is dominated by the 1.65 Ga Obbnäs granites that display signs of tectonic foliation due to the activity of the proximal PMSZ (Kosunen, 1999; Heeremans and Wijbrans, 1999).

Nordbäck et al., (2023) concluded that the main foliation around the study area shifts from WNW-WSE in the west (referred to as Kopparnäs West in the study), to roughly E-W in the center (referred to as Kopparnäs East in the study). According to Nordbäck et al. (2023), the pattern E-W to ENE-WSW ductile shear zones, and NE-SW, N-S, and E-W trending fault zones in the Helsinki area (described by Elminen et al., 2008) are evident on the west side of the PMZ. The study conducted in this thesis focuses on the area around two lineaments trending NE-SW and ENE-WSW presented in fig. 6.

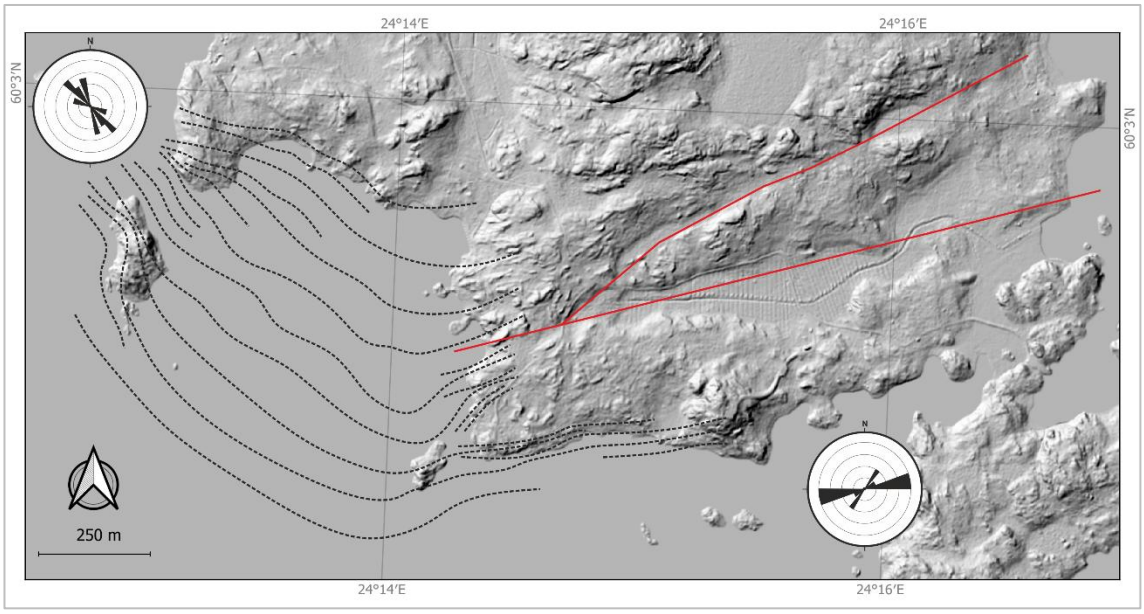

Fig. 6. The study area. Foliation form lines (dashed lines), and foliation rose plots modified from Nordbäck et al. (2023). Red lines indicate lineaments that this study focuses around (Background map: Maanmittauslaitos, 2022).

3 Data and methods

The data used in this thesis is largely provided by GTK. These include 7 electric resistance tomography (ERT) measurement lines, a set of field fracture measurements, 6 ground penetrating radar (GPR) survey lines, optical- and acoustic borehole images (OBI/ABI) of the R307 borehole, OBI/ABI derived numerical fracture data along the borehole, and a borehole ground penetrating radar (BHGPR) image. In addition, a host of supporting open-source data was used, including digital elevation models (Maanmittauslaitos, 2022), aeromagnetic anomaly maps (Geologian Tutkimuskeskus, 2016) and bedrock maps (Geologian Tutkimuskeskus, 2022). Additionally, a field excursion was conducted on the 23rd of April 2025 where complementary measurements were taken. Data provided by GTK is presented in table 1 and fig. 7.

The modelling was done in two phases, referred to as the regional- and the borehole workflow. The results of these phases were then combined into a complete geological model. The 3D modeling was done using the MOVE software by PE Ltd. Lineament interpretations and 2D local analysis were conducted using QGIS.

Table 1. Data provided by GTK

Data	Workflow	Date	Info
Field data	Regional	2022 & 2023	1 172 fracture measurements in total
GPR	Regional	2023 & 2024	9 lines in total.
ERT	Regional	2022 & 2023	7 pseudosections in total.
OBI/ABI	Borehole	2024	From hole R307.
Borehole dips	Borehole	2024	Based on OBI/ABI.
BHGPR	Borehole	2024	Borehole GPR of R307

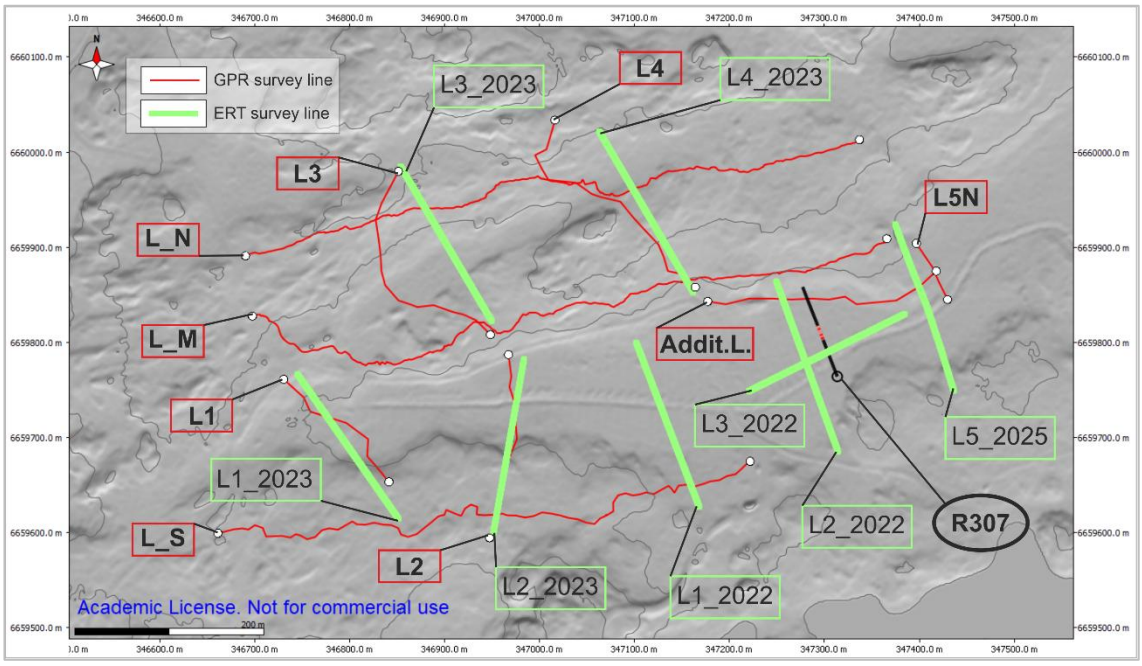

Fig 7. GPR- and ERT survey lines and the location of borehole R307.

3.1 Remote sensing

Aeromagnetic anomalies can be used to trace the ductile continuous structures on a larger scale, whereas the brittle structures can be interpreted from digital elevation models. The magnetic minima and maxima are visible in aeromagnetic images due to the circulation of magnetically reducing or enriching fluids within faults and shear zones. In addition, the breaks in these continuous signals can be considered faulting induced discontinuities in bedrock (Middleton et al., 2015; Engström et al., 2025) Shear zones, faults and high magnitude of shear fracturing can be observed as topographic depressions in digital elevation models (Skyttä et al., 2015; Ruuska et al., 2025 and references therein).

To complement the data given to this model, lineament interpretation of a local scale was done using a combination of existing datasets and publications. For this study, the 50x50m greyscale aeromagnetic raster (Geologian Tutkimuskeskus, 2016) and a 2x2m elevation model (Maanmittauslaitos; 2022) was used. The aeromagnetic images were used to constrain the trends of ductile precursors that may control further deformation. The topographic map was used to constrain the main directions of background fracturing together with the field measurements.

3.2 Field mapping

A dataset of fracture measurements was provided, which consisted of a total of 1 172 measurements containing location, dip, and dip direction information. After filtering the data along the study area, 524 remained distributed on the northern side, between and on the southern side of the lineaments. Reports were written by Sefra Dahlgren and Emma Moen on the field campaigns in 2022 and 2023. The reports included descriptions of fracturing characteristics, regional trends of fracturing orientations and variation of fracturing within different lithologies, which helped with data characterization and interpretation.

A field excursion was also organized in order to visit key locations in the study area. The aim was to assess the characteristics of brittle structures and complement the numerical field data. In essence, fracturing considered here were the foliation parallel primary fracturing, deviating upright secondary fracturing, and the horizontal fracturing. In addition, the walls of the fault zones were measured.

3.3 Electrical Resistance Tomography

3.3.1 Theory

Electrical resistance tomography (ERT) is a method that measures relative resistance values below the ground surface. It is based on the differences of conductivity in geological materials that depend on for example rock type, porosity, weathering degree, water content, and fracturing (Hasan et al., 2021). The method works by passing a current

of controlled intensity through two electrodes (C1 and C2) into the ground and measuring the voltage difference between two potential electrodes (P1 and P2), from which the resulting apparent resistivities can then be calculated (Niculescu and Andrei, 2021; fig. 8). A large number of measurements are taken along a survey line and presented as a pseudosection of measured apparent resistivities, providing an approximation of resistivity distribution underground (Hasan et al., 2021; Niculesu and Andrei, 2021). Inversion programs are needed to convert the relative resistivity values into values of true resistivity, from which geological interpretations can be made (Loke, 2022). A host of different electrode arrays exist that produce different pseudosections of the same structure. One such array is known as the multiple-gradient array, where the current electrodes are kept stationary at the ends of the survey lines and only the potential electrodes are moved at an interval of minimum electrode spacing "a" (Aizebeokhai and Oyeyemi, 2014). Other factors include the separation factor that defines the maximum number of measurements possible for a given current injection "s", relative spacing of potential electrode and closest current electrode "n", the midpoint of the potential dipole relative to the midpoint of the two current electrodes "m" (fig. 8). The best-suited array depends on the geological structure to be mapped, as well as the sensitivity of the resistivity meter and background noise. Things to take into consideration here include the depth of investigation, the array's sensitivity to vertical/horizontal changes in resistivity, horizontal data coverage, and signal strength (Loke, 2022). In general, smaller electrode spacing gives more accurate data but with less depth penetration compared to larger electrode spacing (Huotari and Wennerström, 2017).

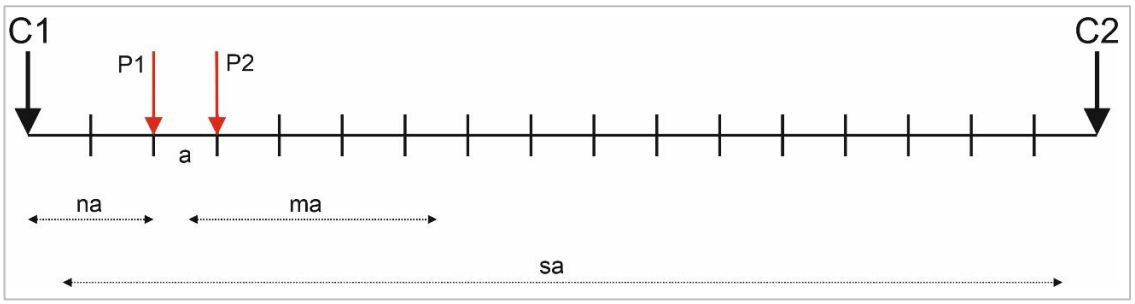

Fig 8. ERT multiple-gradient array. Current electrodes: C1 & C2, potential electrodes: P1 & P2, minimum electrode spacing interval: a, the separation factor (s), the relative spacing between the potential dipole and the closest current electrode: n, position of the midpoint of the potential dipole relative to the midpoint of the two current electrodes: m (Aizebeokhai and Oyeyemi, 2014).

Due to the control of fracturing, weathering, and water content on the resistivity, ERT is well suited to image fault zones in a crystalline bedrock (Hasan et al., 2021). The lowest values represent areas that are for example water saturated, sediment-filled or heavily fractured, which produce significant resistance differences compared to intact bedrock (Hasan et al., 2018; Tao et al., 2022). The method works best in areas where sediment cover is thin, for the low resistivity of the sediment cover prevents the structures within rock masses from being perceived (Huotari and Wennerström, 2017).

3.3.2 Data visualization and interpretation

The ERT data was measured using the multiple gradient array (fig. 8) and the inversion was done by Taija Huotari from GTK using Res2DINV software. The data was imported into MOVE as *point clouds* with each point having a resistivity value. Each *point cloud* was then visualized using the *color map* tool to best display the area of lowest resistivity in the uppermost point layers. The areas of clearest negative anomalies were interpreted to reflect the upper edges of fault zones (fig. 9).

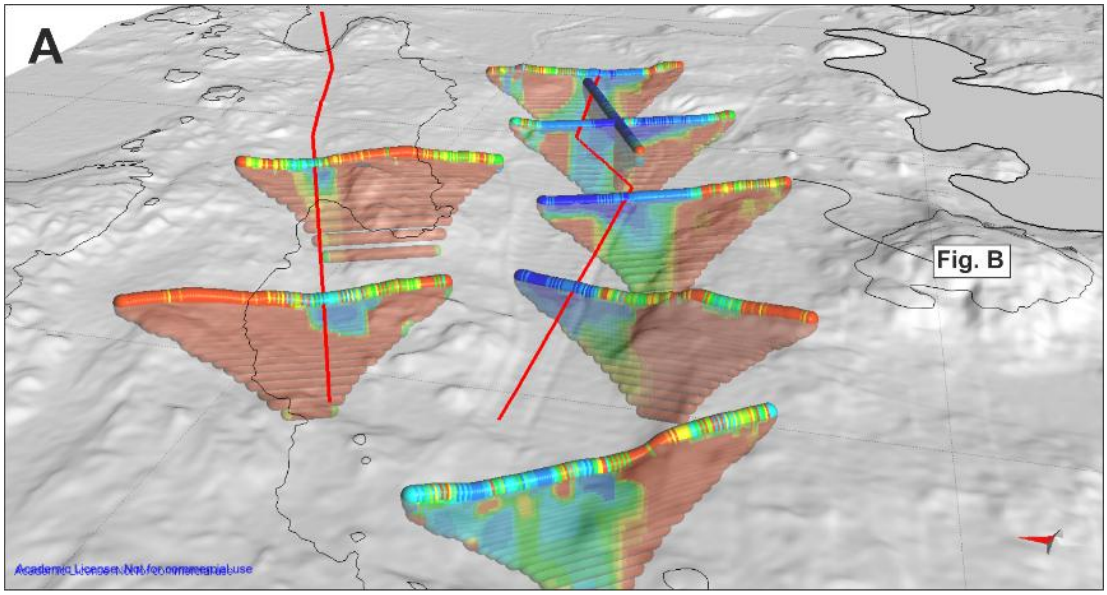

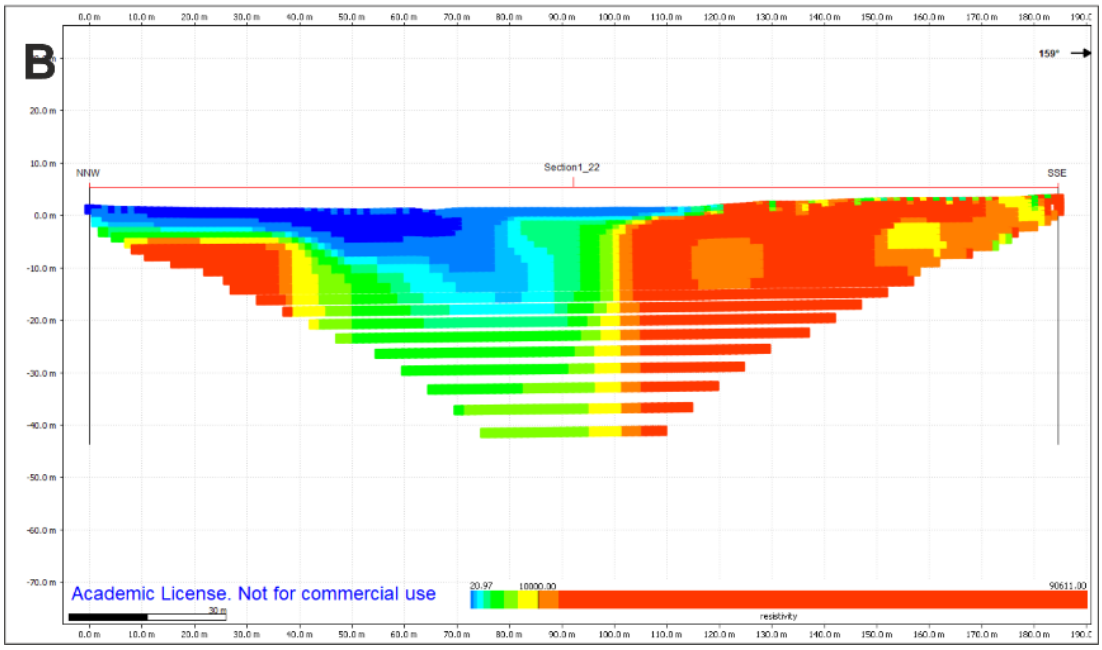

Fig 9. A: All visualized ERT section with interpreted lineaments. B: Section “L1_22” visualized to show points of least resistivity

3.4 Ground penetrating radar

3.4.1 Theory

Ground penetrating radar uses short bursts of electromagnetic (EM) energy around a specified central frequency to image discontinuities in materials (Milsom, 2003). When these EM waves encounter fractures and other inhomogeneities in rock, part of the source energy is reflected back and registered by a receiver antenna (Dorn, 2013; Tao et al., 2022). The time it takes for the reflected waves to reach the receiver is recorded and subsequently used to calculate reflector depths (Walton et al., 2015). Such reflectors are caused by changes in conductivity, magnetic susceptibility, and dielectric permittivity within surveyed material (Walton et al., 2015). In geological materials of low susceptibility, the main parameter controlling wave velocity and reflectivity is the relative permittivity, which for water is considerably higher (around 80) than for most common geological materials (4-6 in granite for instance, Milsom, 2003; Walton et al., 2015; Tao et al., 2022). Relative permittivity depicts a material’s ability to store and release electromagnetic energy relative to vacuum’s ability to do so (Annan, 2008).

Permittivity contrasts, and thus reflectivity within bedrock, can be caused by for example open fractures filled with water or air (Walton et al., 2015). These fractures can be imaged

using the GPR with certain limitations. Imaged fractured must have dips between 0° to 25° (Molron et al., 2020), lie within the depth penetration of the GPR method which depends on the electrical conductivity of the subsurface (Tao et al., 2022) and have apertures larger than the Fresnel zone (Dorn, 2015). The Fresnel zone is the area beneath the transmitter in which the waves are the strongest and its size depends on the frequency of waves, depth to the reflector, and wave velocity in the material. A higher frequency result in smaller Fresnel zone but shallower depth penetration, increased reflector depth results in a wider Fresnel zone and faster moving waves result in a smaller Fresnel zone (Annan, 2003).

GPR data is visualized as a gray-scale vertical section of the subsurface, where the imaged fractures in bedrock appear as continuous high-contrast lines (Milsom 2003; Saksa et al., 2005). The resolution of the GPR data and the depth penetration are dependent on wave frequency and the electrical conductivity of the subsurface respectively (Tao et al., 2022). In general, longer fractures with larger apertures are easier to interpret (Huotari and Wennerström, 2017) but in highly damaged zones, the larger amounts of pore water and high wave scattering make imaging of individual fractures difficult (Dorn, 2015; Walton et al., 2015). Thus, these damaged areas/zones are likely to be detectable as wider areas of energy loss (Walton et al., 2015). It is important to note that the loss of contact with the ground can also cause high reflection patterns, which can be incorrectly interpreted as fracturing (Huotari and Wennerström, 2017). Offsets and discontinuities in reflector surfaces can also be interpreted as fractures (as in Christie et al., 2009) though these can be considered to be more important in areas of sedimentary rocks, where reflection surfaces represent stratified lithological units.

3.4.2 Data visualization and interpretation

A common method of GPR data acquisition was used, where the transmitter and receiver antennas are mounted on the same instrument and moved on the ground surface. The workflow of basic data processing includes i) time to depth conversion, ii) dewowing to remove very low frequency components from the data, iii) assigning the time gain to boost the otherwise indiscernible signals from greater depths and iv) temporal and spatial filtering to better highlight structures to be observed (Annan, 2003; Saksa et al., 2005).

For more detailed descriptions of data processing, see Annan (2003) and Saksa et al. (2005)

The GPR profiles were visualized individually to best display horizontal fracturing. The GPR data was imported into MOVE by creating section traces along the survey lines and the GPR images were then inserted as *vertical images* into the section view and scaled to match their true dimensions in elevation/depth and horizontal extent. The features observed and highlighted in the GPR data can be divided roughly into four categories: 1) wide zones of very high- or scrambled reflection signals, 2) well defined reflection surfaces, 3) discontinuities and offsets of these well-defined reflectors as well as smaller and less well defined reflectors, and 4) small areas of high reflection that begin and end abruptly.

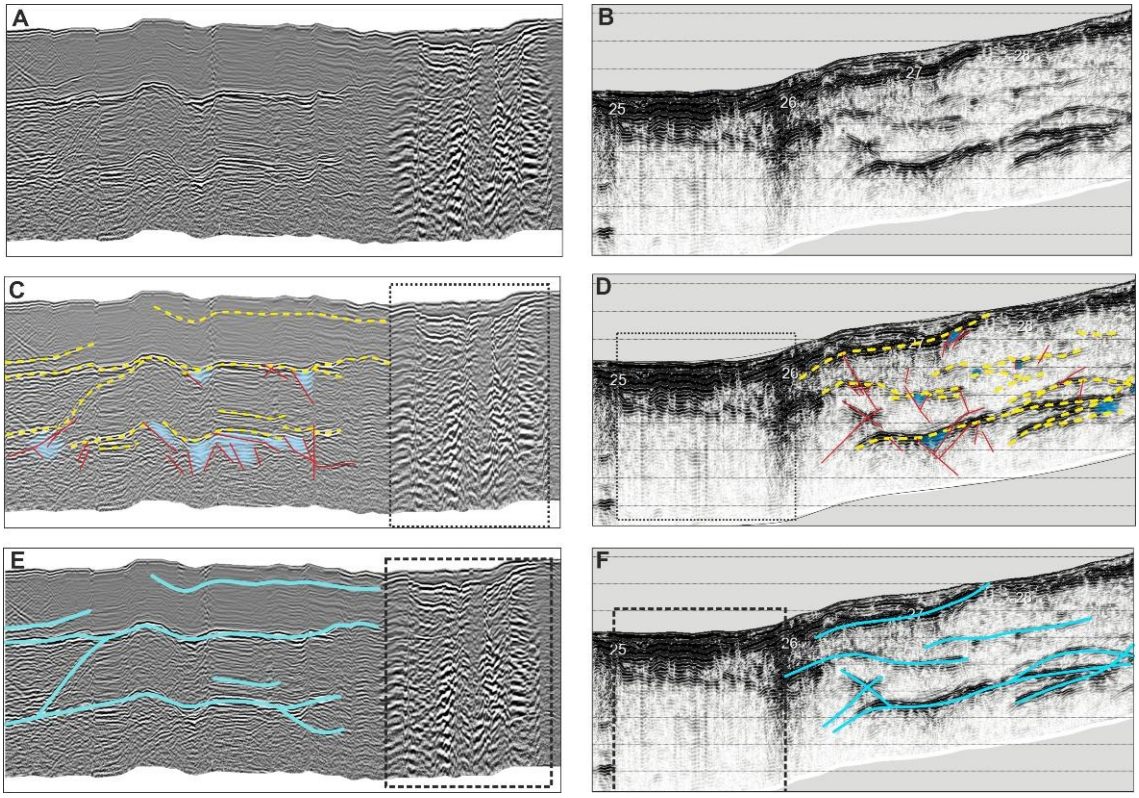

Fig 10. A & B: The two visualization styles of GPR images. C & D: Different signal types highlighted: black dashed box = type 1, yellow dashed line = type 2, solid red lines = type 3 and blue areas = type 4. E & F: Grouped structures of C & D.

Wider areas of energy loss (1) were interpreted to indicate either larger-scale faulting if it coincided with topographic depressions in the DEM, or data loss if the GPR survey line

appeared messy. Using this method, an additional fault was interpreted between GPR lines L3, L_M, and L1 (fig. 11A). Well-defined reflection surfaces (2) were mainly interpreted to be joints and fractures, with the more prominent ones thought to be fractures filled with fluids due to water's high permittivity (Annan, 2003; Markovaara-Koivisto et al., 2014). The horizontal reflection surface discontinuities (3) were interpreted to be fractures with vertical to subvertical apparent dips that abut, crosscut, and connect larger horizontal fractures and fracture systems (fig. 10 C&D). On multiple occasions, these vertical discontinuities host subareas between them that have an appearance similar to the fluid-filled horizontal fractures (4). These were interpreted to be fluid-filled broken zones or series of smaller sporadically oriented fractures. Category 4 signals are also reminiscent of signals from orthogonal fracture systems presented in Song et al. (2025). For the purposes of modelling and due to the uncertainty regarding the origin of signal categories 3 and 4, the connected systems of seemingly permeable environments were grouped together and treated as singular structures. Consequently, a large part of category 4 structures (and some category 3 structures) is merged into category 2 structures (fig 11).

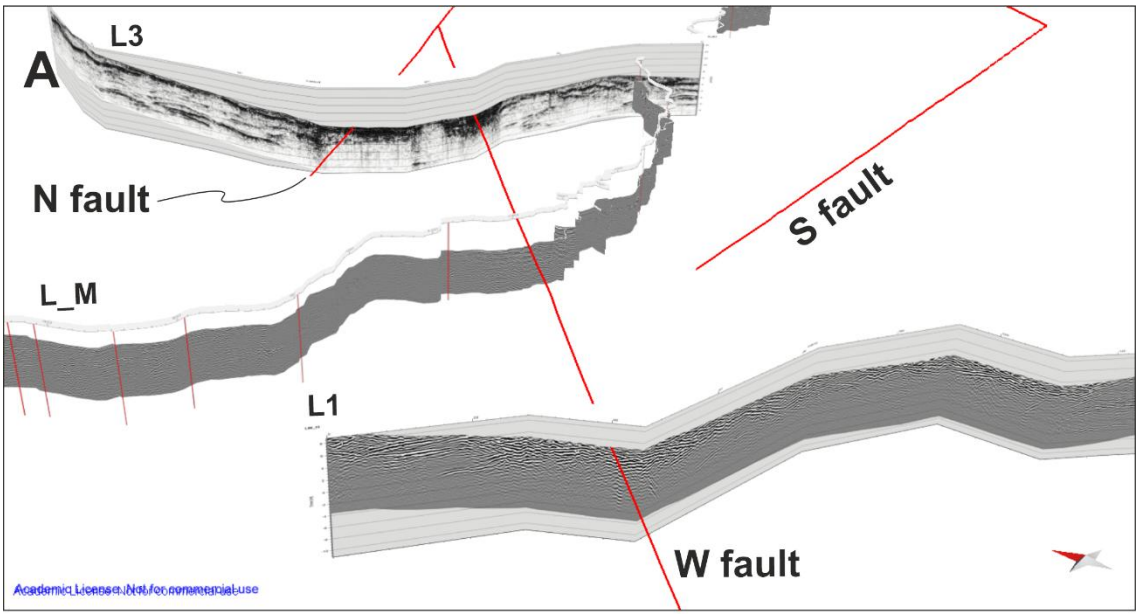

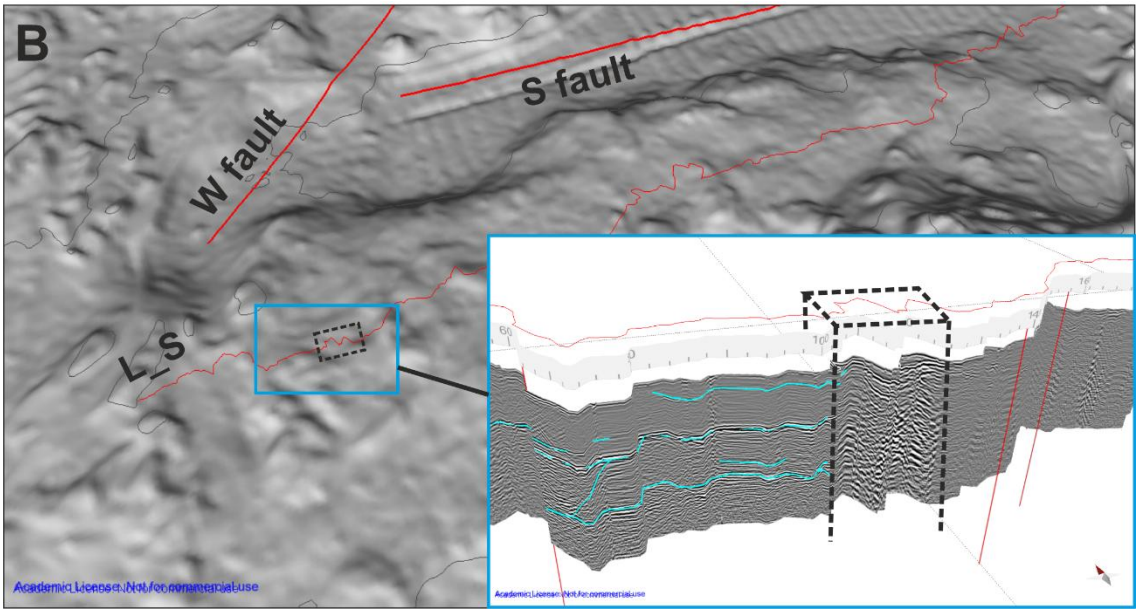

Fig. 11. Examples of DEM and GPR signal comparisons A: identification of W fault with type 1 signals on L1, L_M and L3. B: type 1 signal concurrent with a squiggle in the survey line.

3.4.3 Fracture surface construction (GPR)

The construction of 3D fracture surface was conducted in areas where GPR survey lines intersect (referred here as type A planes) or run close and parallel to each other (referred here as type B planes).

For crosscutting GPR images, the digitized fracture traces are connected or nearly connected in depth, making it easier to interpret which structures are corresponding. By extension, their orientation and dimensions are more easily determined as well, since the digitized fracture lines can be considered as the “skeleton” of the fracture plane, which determines the dip and dip direction as well as the length and width of the plane. The planes’ true dimensions cannot exceed this “skeleton”, for otherwise, it would be observed in the GPR images. The linear *create surface from lines* tool could not be used for these types of fractures. The planes this tool create are asymmetrical, and slight differences in fracture trace elevations cause the surface to fold over itself at the crossing point. Extending the asymmetrical fracture planes using the grid based *extend surface* tool does not take the plane surface morphology into consideration and creates an unrealistic appendix. The *extend up/down dip* extrudes surfaces while considering the existing surface morphology but this tool usually extends the surfaces beyond the fracture plane “skeletons”, making it unsuitable for this purpose. *Delaunay triangulation* and *B-spline*

curves were also tested for this purpose. Triangulation works best for more evenly spaced point clouds and proper triangles could not really be formed here. B-spline, on the other hand, does not follow the "skeleton" properly and the surface morphology was off. For these reasons, the *Ordinary kriging* interpolation method was used to create all type A surfaces. For interpolation, fracture lines were collected to be used as the base data of interpolation, and the planes were interpolated using a symmetrical grid. The quadrant search parameters were adjusted to keep the resolution high enough so that the plane follows the "skeletons" without forming any major gaps (fig. 12).

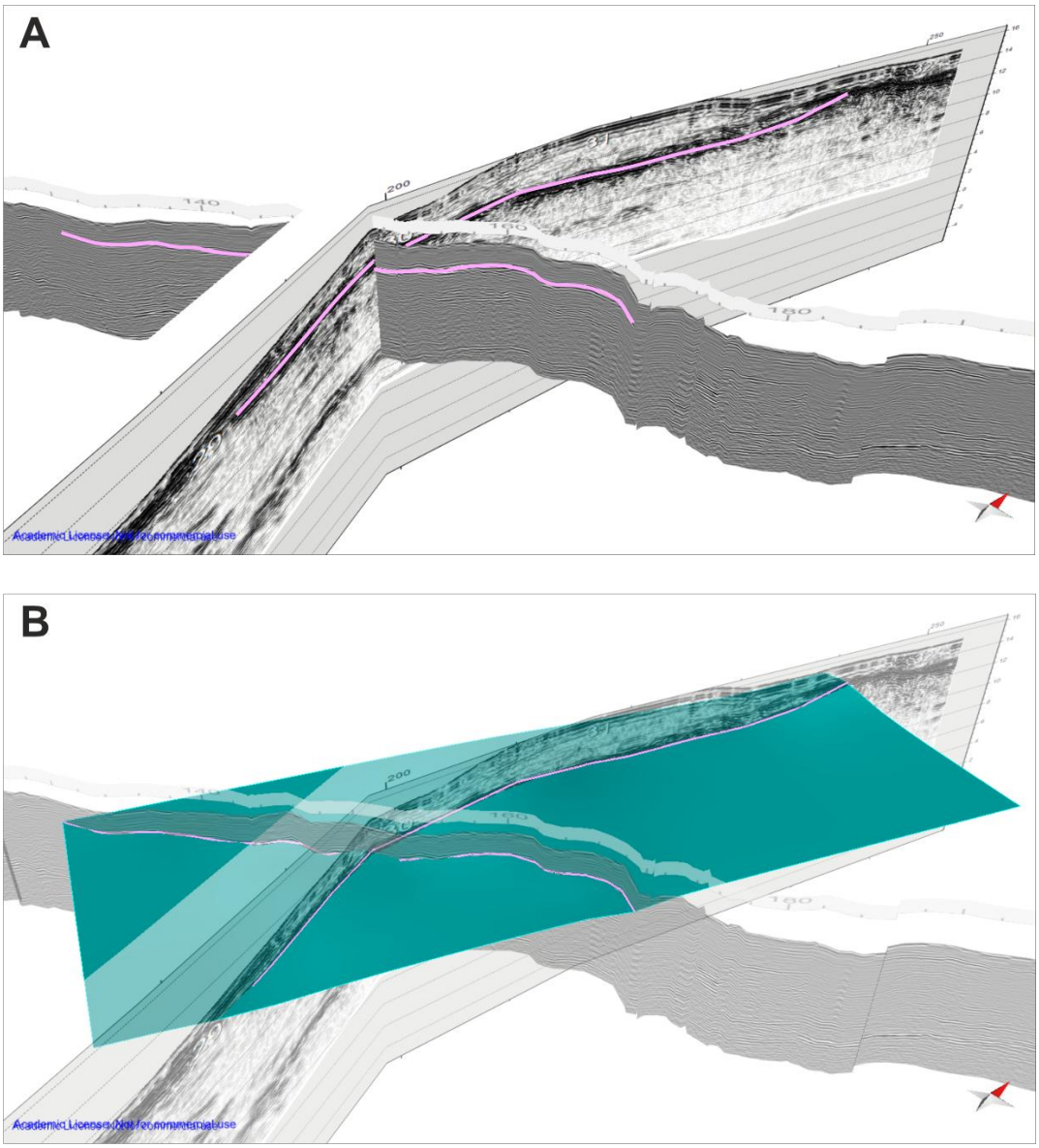

Fig. 12. Type A fracture surface. Violet traces = corresponding fracture lines that form the plane "skeleton". Note that the plane cannot extend in any direction symmetrically, without exceeding trace boundaries.

For parallel GPR images, geometrical fracture systems were compared to each other in order to ensure that the formed surfaces represent the same fractures. In a fracture system, the same fracture can be distinguished in two parallel GPR images. These can then be connected with the linear *surface from lines* tool and further extended to a symmetrical surface. In this method, the orientations and especially the dimensions of the fracture surfaces were harder to quantify. Ends of the reflection (or fracture) traces in the GPR data can be considered as "exit points" by which the fracture planes must abide even if the orientation of the reflection surface (or fracture) remains uncertain beyond and between the GPR lines. First, the lines were connected into a surface linearly, which provides the orientational properties of the surface. Secondly, the *extrude up/down dip* was used to conserve the original dips and dip directions of the created asymmetrical planes. In some cases, the surface could not extend beyond the GPR data due to the orientation. In other cases, the surface could theoretically extend much further than the GPR line. In the latter instances, surfaces were extended in reasonable amounts beyond the GPR lines to avoid excessive extrapolation (fig. 13).

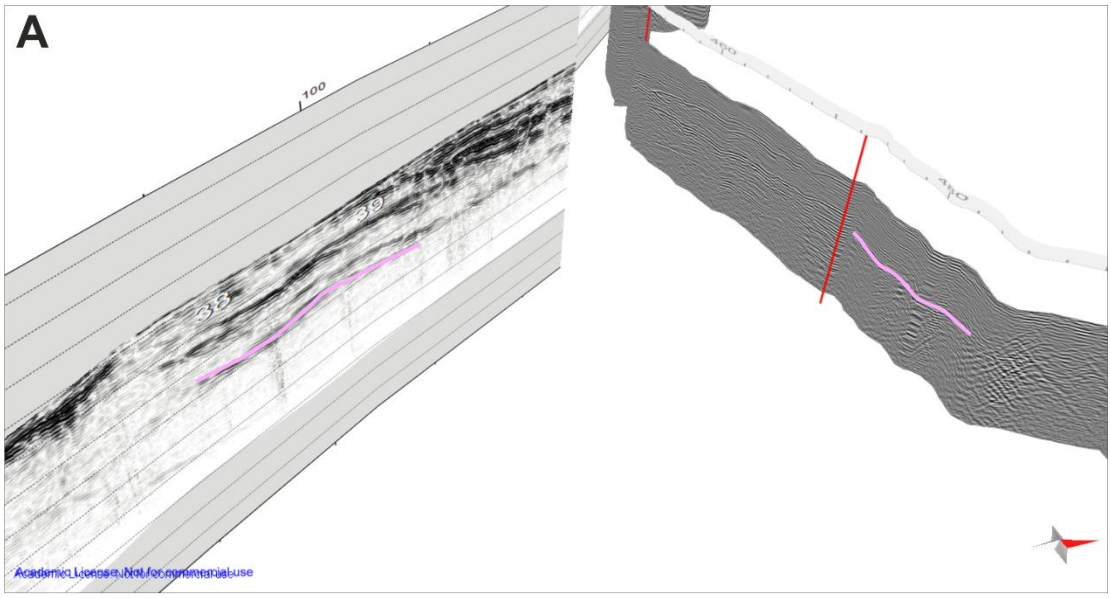

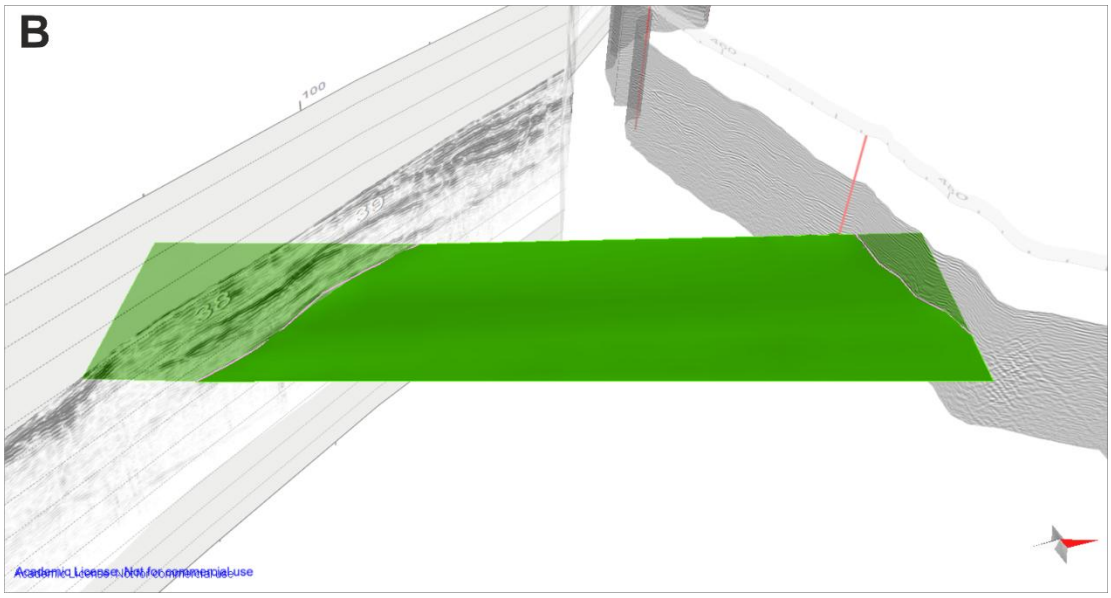

Fig. 13. Type B fracture surface. Note that due to the rectangular shape, the plane cannot extend towards the north but could theoretically be extended further in the southern end.

There were some exceptions to the above-mentioned methods, since some of the type B fractures could not be formed with the *surface from lines* tool or the subsequent extension was impossible. In the latter situation, the extended parts of the surfaces did not follow the dip and dip direction of the plane and/or had an unnatural surface morphology. In these instances, the surfaces were interpolated using *Ordinary Kriging* similarly to type A planes.

3.4.4 Data conditioning and analysis

After the surfaces were constructed, they were resampled to the original triangle count so that further conditioning and analysis would be possible. Some of the interpolated surfaces had minor holes at the edges, which were fixed with the *fill holes* command by using the proximal ends of the mesh triangles. Some unnatural depressions or spikes in the surfaces were also fixed by manually deleting the anomalous grid points and then filled back up using the *fill holes* command (fig. 14). The fracture surfaces were split, merged and trimmed to match the crosscutting relationships visible in the GPR images for type B fractures.

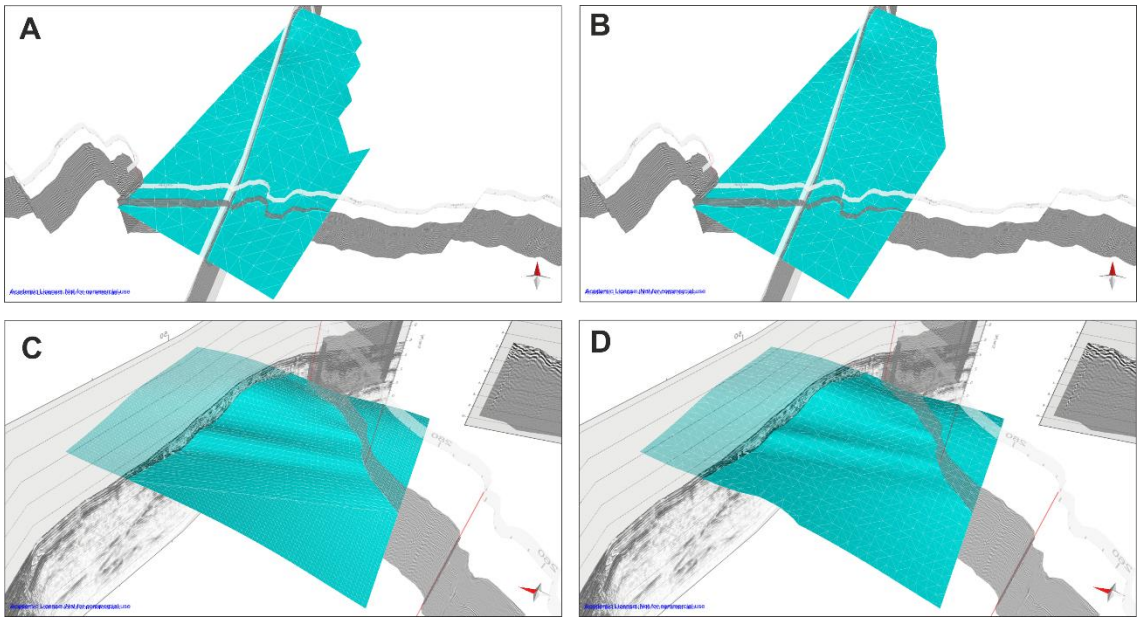

Fig. 14. A & C: unconditioned surfaces. B: Filled holes using the edit tool. D: Resampled to a matching triangle count.

3.5 Borehole ground penetrating radar

3.5.1 Theory

The basic working principle of the BHGPR is the same as in the surface GPR. Radio waves are transmitted into material, and discontinuities and other heterogeneities reflect the waves back which are then picked up by the receiver. The difference here is that BHGPR is used by lowering the apparatus into a borehole as opposed to it being dragged along the surface. The same limitations still affect BHGPR considering for example the wave propagation and the incapability to detect certain fracture orientations in relation to the instrument (Dorn et al., 2012).

The BHGPR instrument has a separate transmitter and receiver that are set at a fixed length apart and lowered into the borehole. Pulses of radio waves are then transmitted at a regular interval as the instrument is lowered along the borehole (Olsson et al., 1992; Serzu et al., 2004). The basic principle of result display is the same as in the surface GPR, where position along survey line is presented on the X axis and the travel time is presented on the Y axis. The two different types of reflection signals include parabolas from point reflectors and traces from planar reflectors (fig. 15). Planar reflectors that cross the borehole are presented as two branched traces, for the boreholes pass through the fractures and both ends of the plane are imaged (Olsson et al., 1992, fig. 15). Commonly used

borehole antennas poorly constrain azimuths of imaged reflectors since the imaging is restricted to omnidirectional radiation patterns around the borehole axis (Olsson et al., 1992; Dorn et al., 2012). In general, the BHGPR as a method is used to map the fractures and fracture zones at greater depths (at best 100s of meters), whereas the surface GPR is used to map fractures at some 10-20m depth (Dorn et al., 2012). In addition, BHGPR is usually used to map more vertically oriented fractures, especially in steeply dipping boreholes, since the imagery is practically limited to dips between 30° and 90° for vertical boreholes.

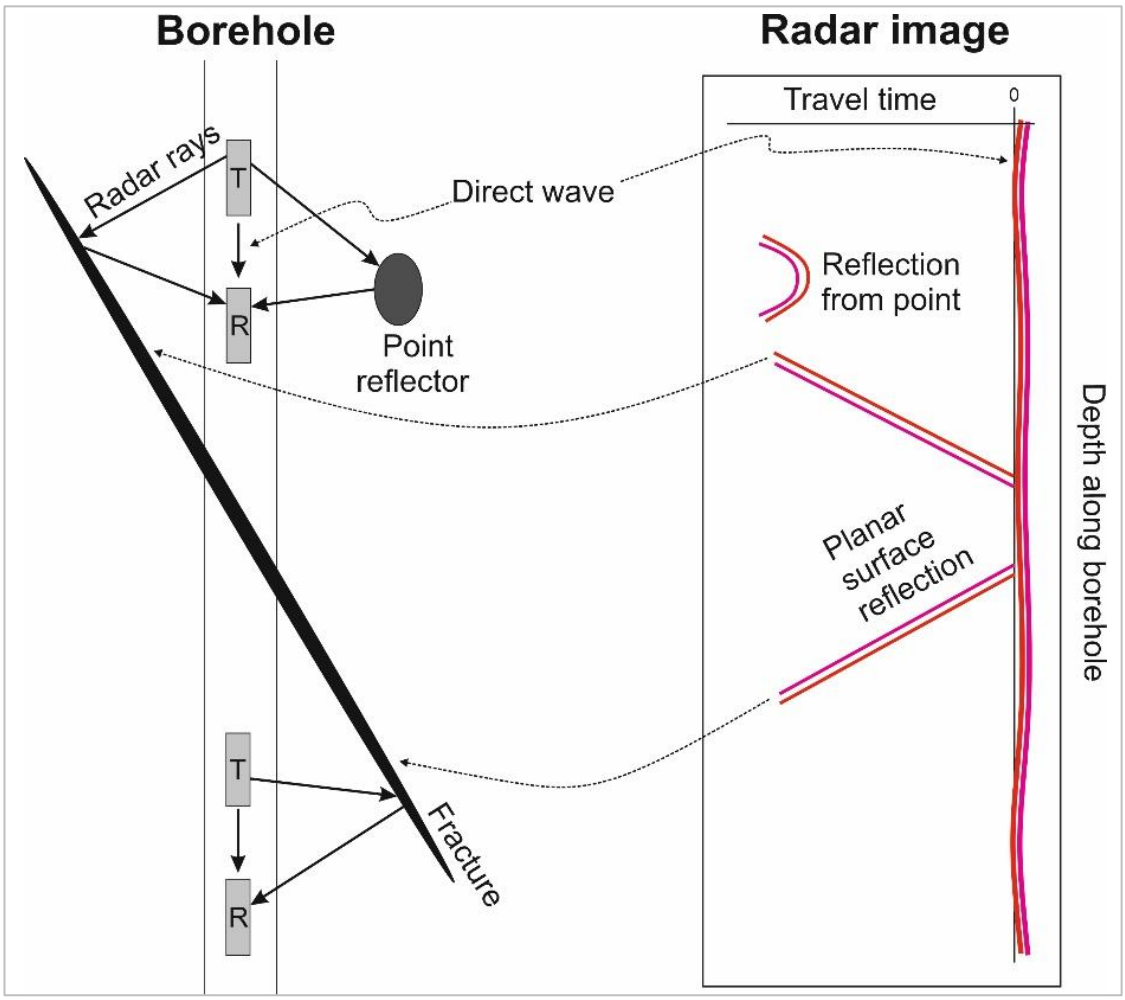

Fig 15. Borehole GPR instrumentation and reflection signals (Modified from Olsson et al., 1992).

The borehole GPR used in this thesis was gathered with the Malå borehole system using 100 MHz and 250 MHz frequencies in August 2024. The 250 MHz image was chosen for further work since fractures were more prominent here. Processing was done by Petri Valasti from GTK. Time zero correction was set at 14.4 ns and epsilon at 6.3. The 250

MHz survey was done from bottom to top and at each depth interval the transmitter stayed at a fixed position. A total of 9 intervals were measured.

3.5.2 Fracture surface construction (BHGPR)

The borehole R307 was imported into MOVE using collar location, track length and track direction data. The OBI/ABI-based numerical fracture data was imported along the borehole as *dip data,* creating the dataset “true dip data” in MOVE (fig. 16). A *section trace* was constructed in the direction of the borehole, and the borehole track and true dip data were then projected onto the created section. When projecting data onto a section, MOVE creates a separate dataset that hosts apparent properties of the two-dimensional cross section, creating a separated dataset “projected dip data” in MOVE. This meant that for the projected dip data, the orientation properties do not match the real dip and dip direction values. In the *attribute table*, the rest of the attributes are inherited from the true dip data (measured depth, aperture size, type etc.) which can be applied to link the corresponding projected dip markers and true dip markers with each other.

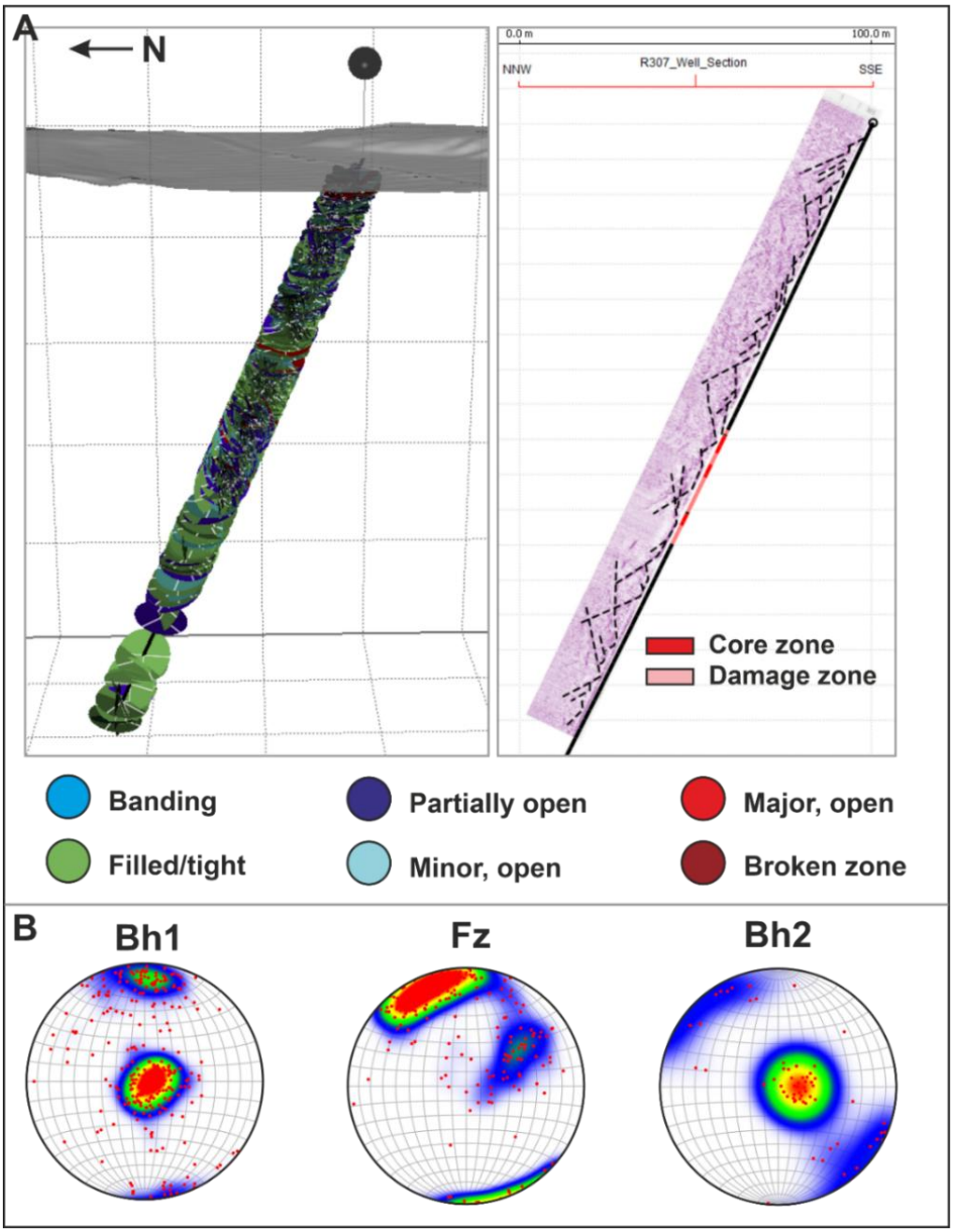

Fig 16. A, left: borehole survey and imported true dip data, right: fitted borehole GPR image and fracture traces (black dashed lines), bottom: dip coloring scheme of dip markers based on fracture aperture hierarchy. B: borehole dip data of Bh1, Fz and Bh2.

GPR fracture traces were interpreted onto a horizontal image using CorelDRAW, focusing on two tailed reflectors that intersect the borehole. The annotated figure was imported, scaled, and rotated using the *basic transformation* tool to match its true dimensions and the annotations were drawn over in the *section view* using the *create line* tool (fig. 16). Line objects in MOVE have a unique value that can be observed from the *object attributes*. The lengths of these fracture traces in Borehole GPR can be considered

as the diameters of fracture surfaces. Previous work on R307 (e.g., Engström et al., 2024) concluded the borehole is intersected by a fault that has three distinct core zones separated and surrounded by damage zones. The combination of these core and damage zones is referred to here as the fault zone (Fz), the interval above the Fz is referred to as Bh1, and the interval below as Bh2 (fig. 16).

To construct fracture planes, the following workflow was carried out:

1) *Point data* were created at depths along the borehole track where a projected dip marker and an intersecting fracture trace coincided, creating the "fracture points" point cloud.

2) Fracture points were automatically assigned a Z value, representing true depths of fractures, and inherited values for each point were assigned from the projected dip data.

3) The dip and dip direction values for each fracture point was assigned individually from the true dip data, using the inherited attributes and the Z values to link corresponding fracture points and true dip markers.

4) The fracture diameter attribute was assigned from the length of the corresponding fracture trace.

5) A MOVE *fracture set,* and a *vertex cloud* were created from the fracture points using the *create fracture set* and *create vertex cloud* tools respectively.

6) For the *fracture set*, the orientational data was assigned automatically from the attribute table, *length* was assigned from the diameter attribute and aspect ratio was set to 1.

7) A *dip dataset* was created from the *vertex cloud* with each dip marker scaled to true dimensions using the *quick editor*. The results are presented in chapter 4.4.

A general hierarchy by which the dip and dip direction values were assigned for fracture points was based on the aperture size of the true dip data points. Dip markers with largest assigned aperture sizes were considered primarily when assigning the dip and dip direction to a point. The nature of fracturing was also examined from OBI/ABI images for each of the fracture points to make sure that major fractures or sets of fractures were

considered. In situations where there were multiple fractures with similar apertures, the one that appeared more prominent on the OBI/ABI data was considered. Examples of aperture considerations are presented in fig. 17.

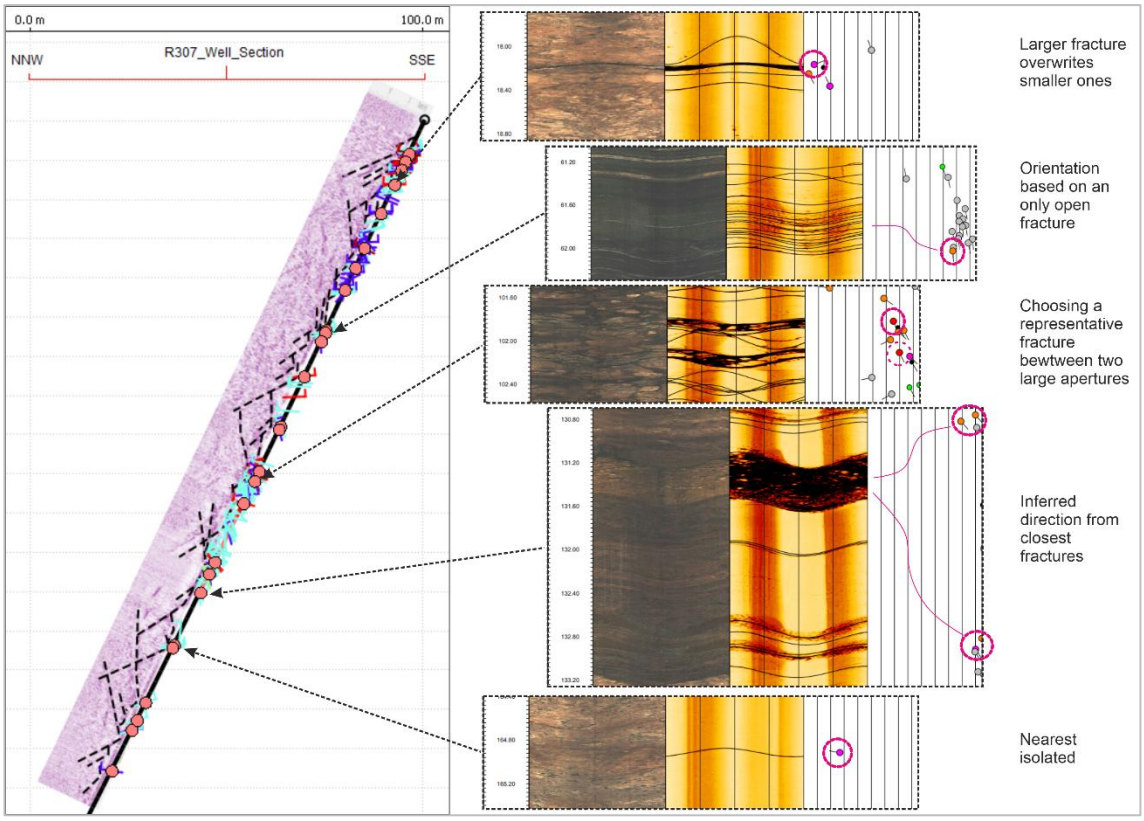

Fig. 17. Workflow of fracture surface construction. All intersections of fracture traces (beige points), projected dip markers i.e. projected dip data, and examples of crossreferenced OBI/ABI images. For aperture coloring scheme see Fig 16.

4 Result

4.1 Remote sensing and field data

A broad investigation was done for the continuous trends of magnetic anomalies around the study area. Three general trends near the vicinity of the study area were observed in the aeromagnetic images: NW-SE to the west of the study area, E-W at the study area and NE-SW to the east of the study area. In addition, some relatively tight folded patterns were also identified. The general summary includes the orientational trends to curve into a “cup-like” shape around the study area (fig. 18). DEM was used to trace smaller linear forms near the main lineament. These lineaments show strong E-W to ENE-WSW

striking trends, however more NE directed individual lineaments are also present along with some NW striking traces. Most of the traces are focused on the western edge of the study area, with the eastern and southeastern parts being scarcest.

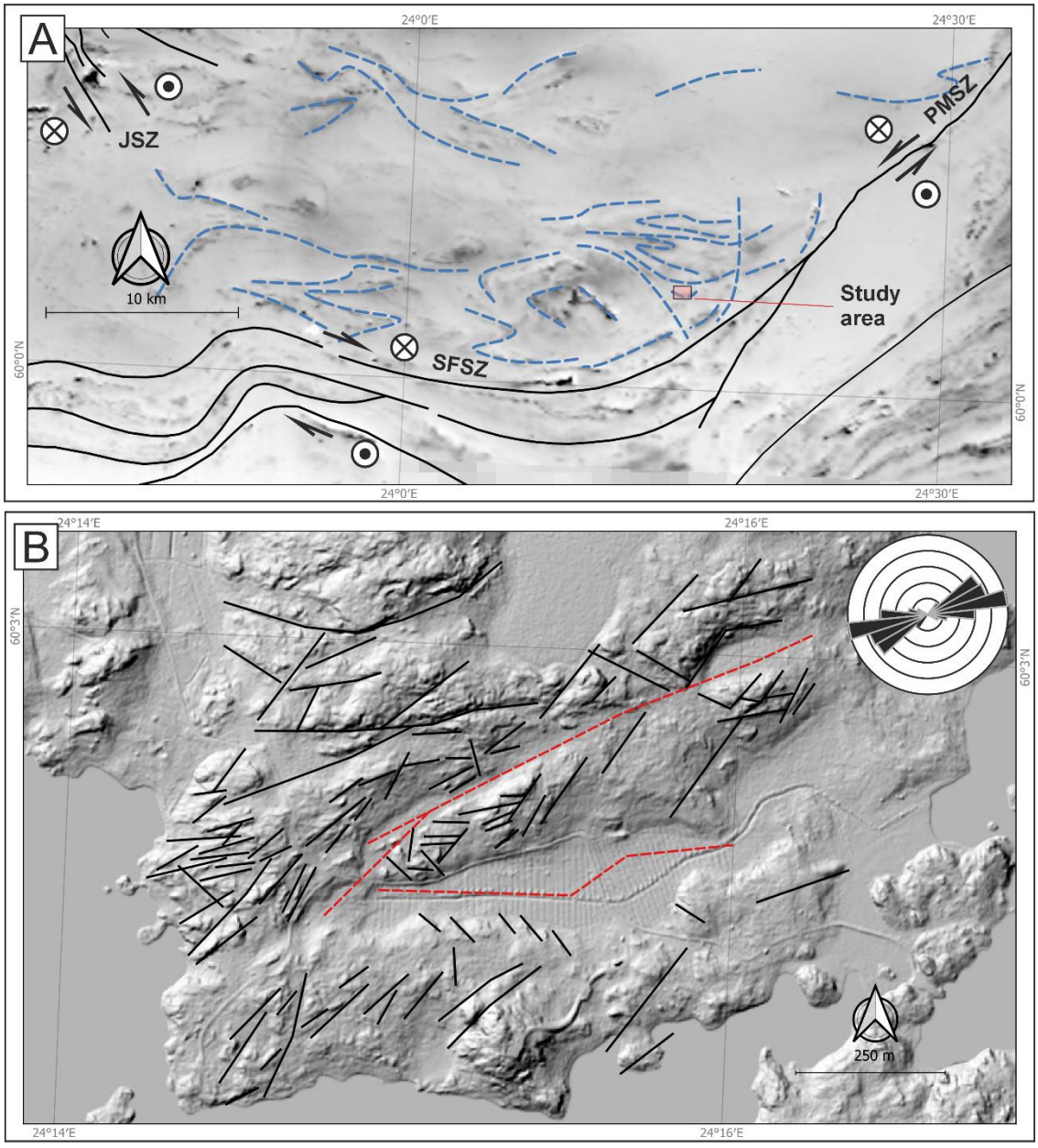

Fig 18. A: Large ductile trendlines from aeromagnetic images. Proximal shear zones visible (from GTK, 2022) B: DEM based traces of small-scale lineaments and their orientational trends (rose plot).

During the field day conducted in the spring of 2025, the main orientation of fracturing was interpreted to be roughly parallel to the general foliation in the area (E-W to ENE-WSW striking, Nordbäck et al., 2023). A second fracture set was observed deviating from

this orientation, usually striking roughly N-S or NNE-SSW. Subhorizontal fractures were also present, though less abundantly outcropping, as was expected. These orientational trends are also prominent in the field measurements provided by GTK with the main orientation of fracturing being a subvertical S to SE dip (fig. 19 A).

Fracture measurements were divided into three sets, based on their orientation: the most abundant, roughly E-W strike (Set I), roughly N-S striking fractures (Set II), and horizontal to subhorizontal fractures (Set III). The fractures were further filtered to represent measurements around the available geophysical data, where horizontal fractures would be modelled. For these filtered dips, Set II seems more pronounced than Set I. Set III fractures could also be observed here, highlighting the confirmed presence of horizontal fracture set in areas where horizontal fractures were imaged with the surface GPR (fig. 19 B).

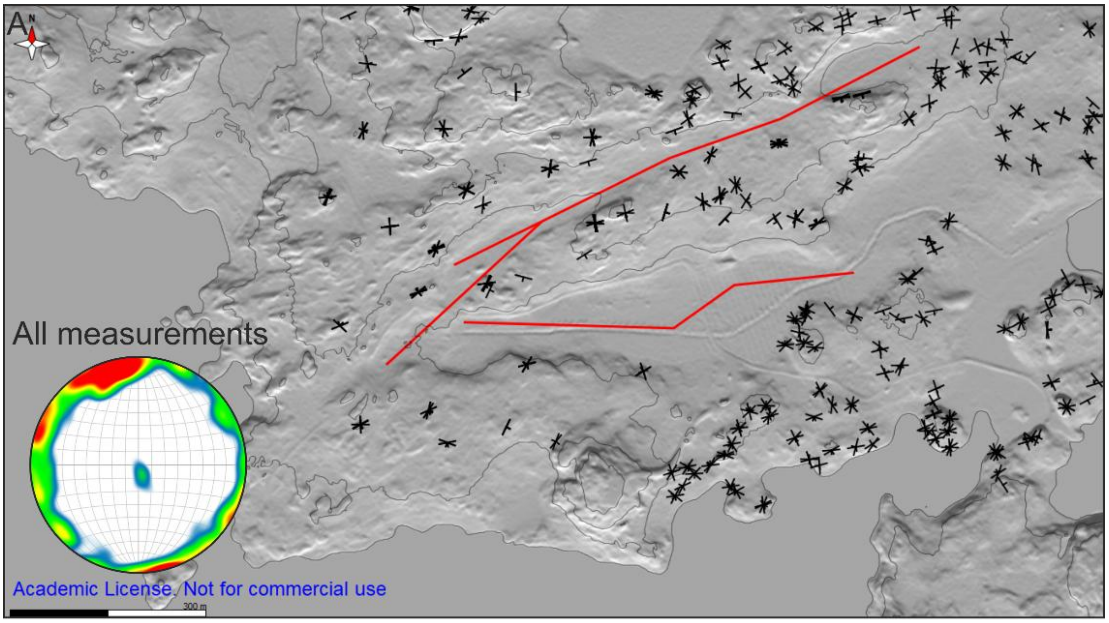

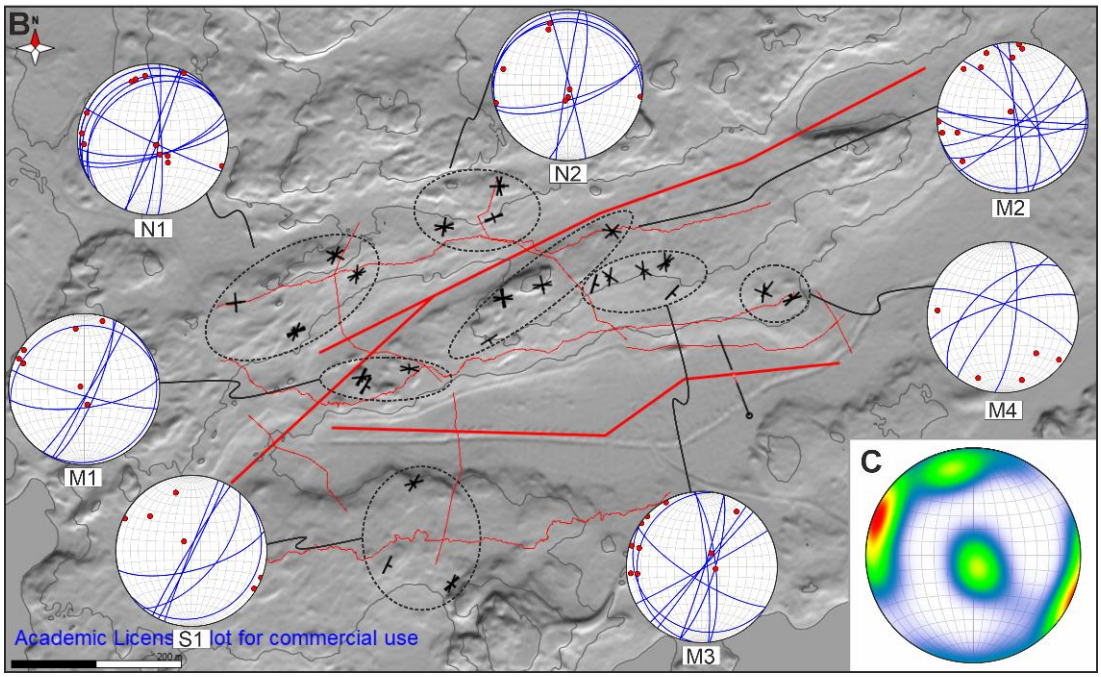

Fig 19. A: all field measurements in MOVE map view and plotted on a stereonet. B: fracture measurements coinciding with areas where GPR fractures could be modelled. For cluster naming scheme see chapter 4.3. C: combined stereonet of the chosen field measured fractures.

4.2 Geometry of the faults

Type 1 structures of the GPR signals were compared with the topographic depressions in the DEM surface. In addition, both were also crossreferenced with the ERT data to get best possible location of the fault planes near the surface. In total three larger fault zones were interpreted from the data: the Northern Fault (NF), the Southern Fault (SF) and the Western Fault (WF) (fig. 20). Orientations of the NF and SF planes were extracted from field observations and the borehole data respectively but no concrete orientational data was available for the WF. Hence, its orientation was inferred from proximal field data. The R307 Fz host open fractures of similar orientations that can be clustered, and the average orientation of these main fractures could be considered to roughly represent the orientation of the fault zone. For regional workflow, these three fault cores were considered as one fault represented by a single plane. An average of all the main fracture orientations was considered to assign average dip and dip direction for the fault plane. NF was found to be outcropping during the field day (23rd of April 2025), and its orientation could be directly measured.

NF is thus oriented at 155/72, SF is oriented at 173/77, and the WF is oriented at 137/71. The lengths of the fault planes are set at a semi arbitrary 787 m, 618 m and 324 m, respectively, since their extents are not exactly known. The faults were only extruded 50 m downward, though at least the southern fault extends to depths of at least 120 m where it intersects the borehole. This was done for modelling purposes, since the GPR depth resolution is around 20 m.

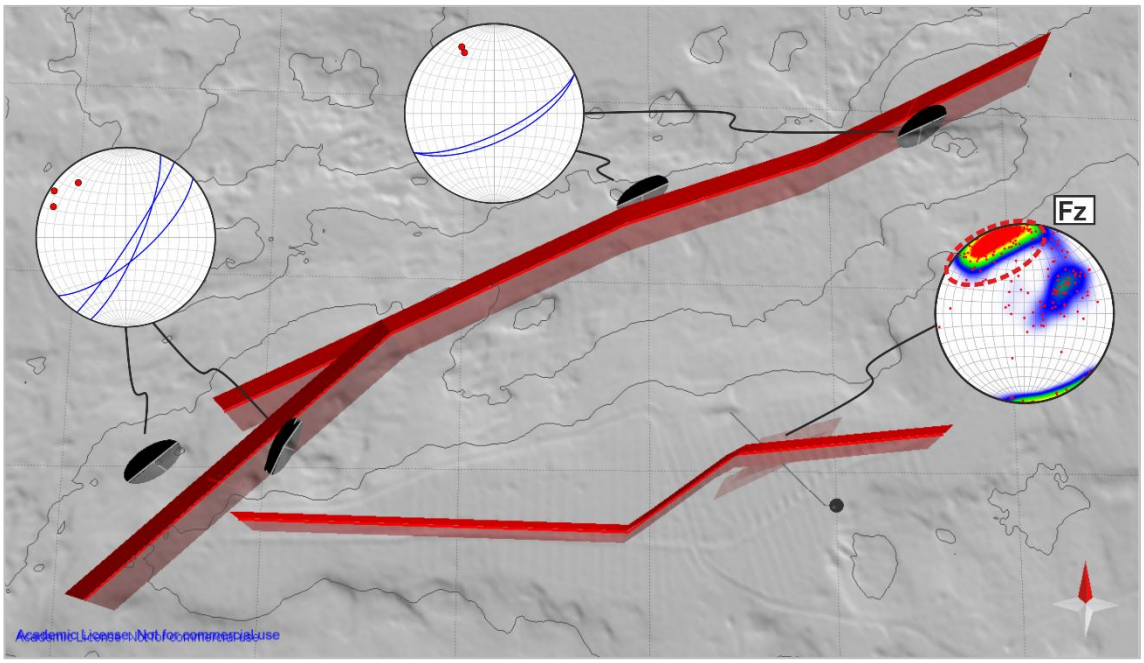

Fig 20. Extrusions of the three fault surfaces.

4.3 GPR fracture surfaces

GPR image interpretation yielded a total of 626 fracture traces across the 9 survey lines. The grouping of the apparent permeable structures resulted in tens of meters long continuous horizontal to subhorizontal fracture traces. From these traces, 113 were used to construct a total of 47 subhorizontal to horizontal fracture planes: 15 on the N side of the faults, 28 in between the NF and SF, and 4 on the S side of the faults. The areal extents of these planes vary from some ten square meters to a couple of thousand square meters (Min: 29 m^2, mean: 673 m^2, Max: 3060 m^2), with the largest diameter being over 50m long. Multiple fracture planes were able to be constructed for each spot, resulting in fracture planes being clustered in certain spots. These clusters were divided into groups

based on their position compared to the faults (fig. 21). Two on the N side of the faults (N1 & N2), four in between NF and SF (M1-M4), and one on the S side of the faults (S1). Below, these are referred to as Northern area, Middle area, and Southern area clusters, respectively.

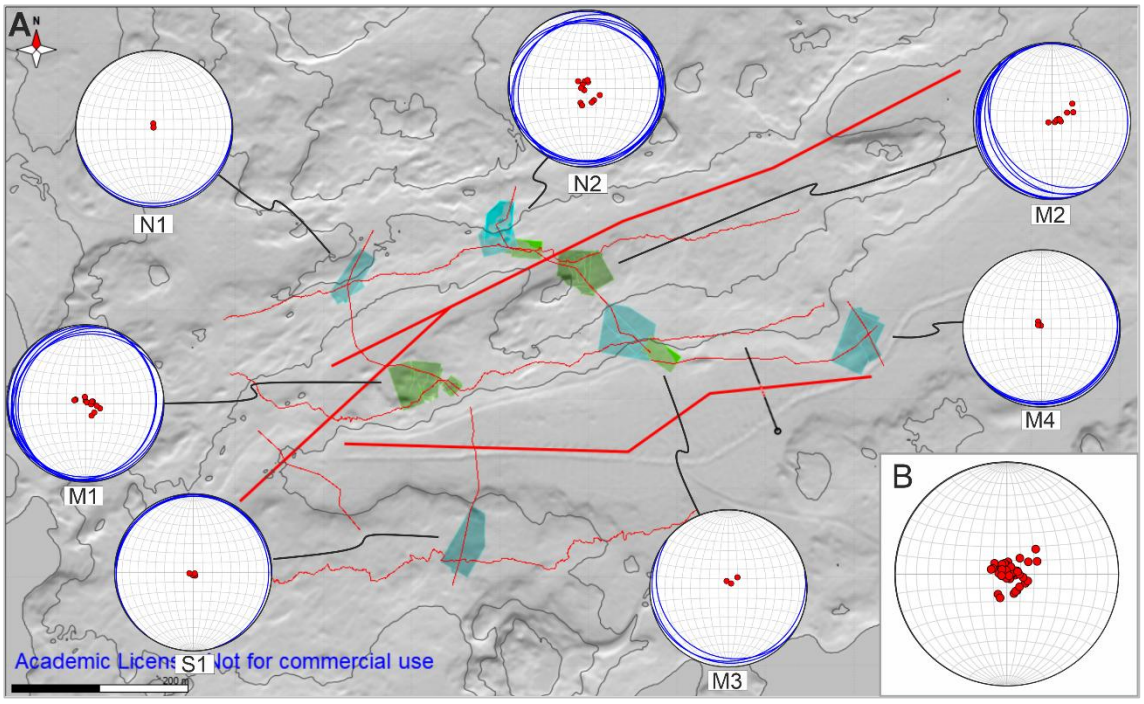

Fig.21. A: Fracture plane cluster locations and the orientations of the planes plotted in stereonets. Blue planes are type A (crossing lines), green planes are type B (parallel lines). B: Stereoplot of all modelled fracture planes.

Northern area clusters

N1 cluster is located somewhat further away from NF while N2 is in immediate proximity to it. All N1 planes are generated at the cutting point of L3 and L_N GPR lines and are thus considered type A planes. N2 is constructed from L4 and L_N and it hosts 10 planes considered as type B, 1 type A plane, and one where a fracture plane could be constructed from a bend in the survey line L4. The GPR lines L4 and L_N are interpreted to cross at a singular point where the type A plane of N2 could be constructed. Eastward of the crossing point, the lines run parallel very close to each other, causing the extrusion of these planes to be estimates (fig. 21, 22). Here, the planes were extruded less than the length of the fracture traces.

Both clusters show general trends of subhorizontal southward dips. N2 hosts some planes that dip somewhat deeper to the north (fig. 21 and 22). Fractures with larger areas are situated closer to the surface, whereas the deeper lying planes are smaller. In N2, the larger fractures are in general also oriented along the surface topography, dipping roughly southwards, whereas the steeper north dipping fractures have smaller areas. For N1, all the planes dip southward towards the fault with no outliers present.

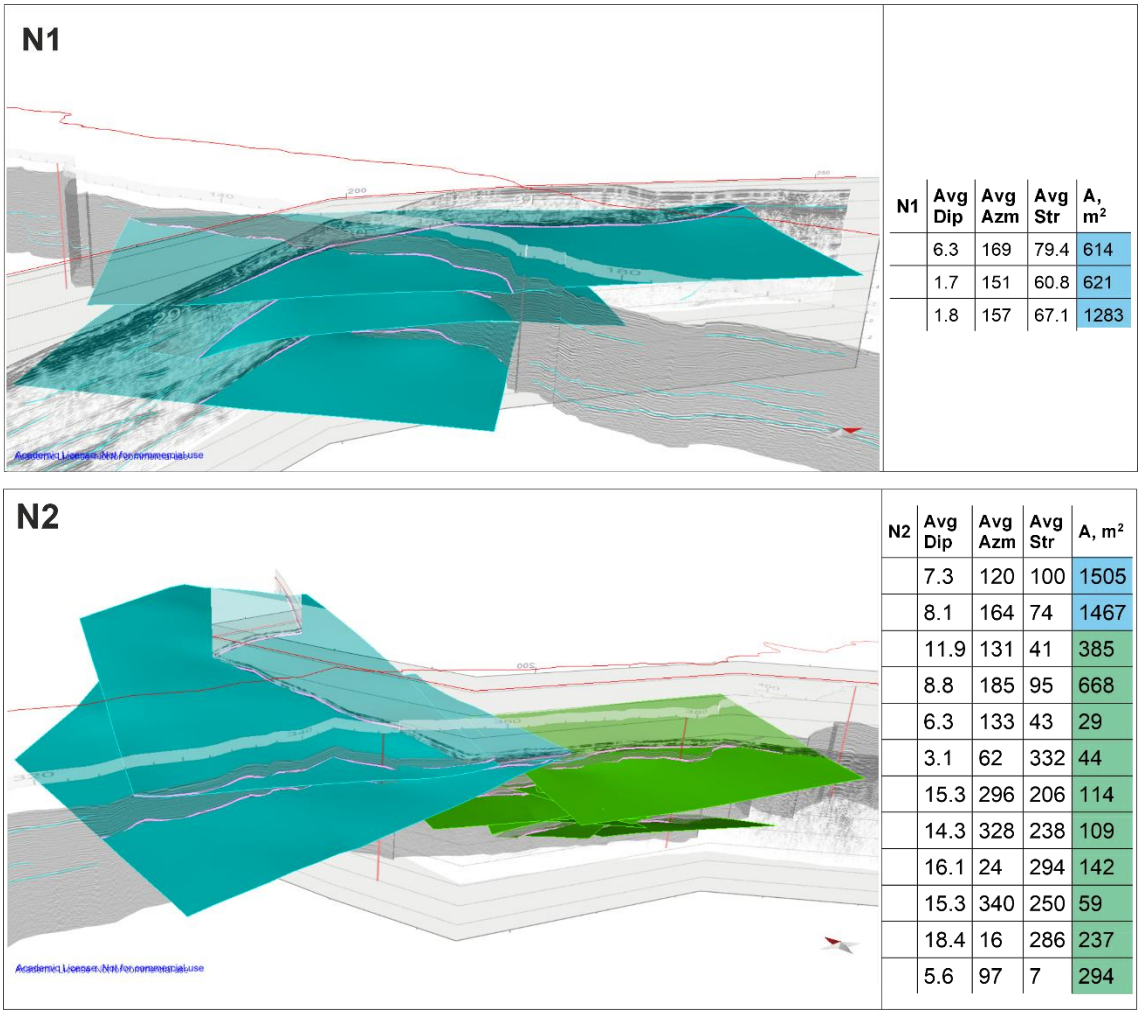

N1	Avg Dip	Avg Azm	Avg Str	A, m²
	6.3	169	79.4	614
	1.7	151	60.8	621
	1.8	157	67.1	1283

N2	Avg Dip	Avg Azm	Avg Str	A, m²
	7.3	120	100	1505
	8.1	164	74	1467
	11.9	131	41	385
	8.8	185	95	668
	6.3	133	43	29
	3.1	62	332	44
	15.3	296	206	114
	14.3	328	238	109
	16.1	24	294	142
	15.3	340	250	59
	18.4	16	286	237
	5.6	97	7	294

Fig 22. Northern clusters N1 & N2, their type (A or B, blue or green respectively) and statistical data on their geometries.

Middle area clusters

Four fracture clusters are situated between the fault planes. This area hosts a significant number of clusters due to the multitude of crosscutting and parallel survey lines. The general trend of larger fractures being situated in the surface layers and oriented along

topography is observed here, though some outliers are also present. The largest fractures are horizontal with the smaller, at times abutting, fractures having steeper dips and more pronounced directional trends.

M1 cluster is situated on the eastern and western sides of the crossing point of L3 and L_M survey lines. It hosts 12 type B planes, one of which was interpolated using the *Ordinary Kriging*. Fractures are considered type B, since none of the traces appear within or on both sides of the crossing point, i.e., they only appear in the parallel running parts of the surveys. L3 and L_M host intricate fracture systems making it easier to determine corresponding traces based on fracture trace orientations and relationships. This subsequently increases the confidence of modelled plane extents, especially on the planes W of the crossing point. M1 fracture planes show trends of subhorizontal dips directed from SW to E with the NW direction seeming most dominant. The largest fractures are situated near the surface (0-4m), though one fracture with an area over 500 m is also situated some 10m underground

M2 cluster is situated immediately on the southern side of NF and is constructed from the parallel run of L4 and L_N. M2 consists of 9 type B planes, 3 of which were interpolated using *Ordinary Kriging*. Like M1, the well visible fracture networks were used to link traces. M2 hosts mainly W to SW dipping fractures, some of which are truncated by NF. Smaller fractures have steeper dips, and the only E dipping outlier also hosts a relatively small surface area. The largest fractures here are situated somewhat deeper underground as opposed to the very surface layers.

M3 is constructed from the crosscutting lines of L4 and L_M as well as the parallel sections of the very western end of the Addit. L. and L_M. Two type A planes and one type B plane could be constructed here. This cluster is situated near the depression of the S fault making the GPR images fuzzy and structures harder to interpret. All M3 fractures have gentle SW dips.

M4 fractures are type A fractures based on the Addit. L. and LN. In total, it hosts four fractures with subhorizontal S dips. The largest fractures are located at a depth of 2 to 10 m (fig. 23).

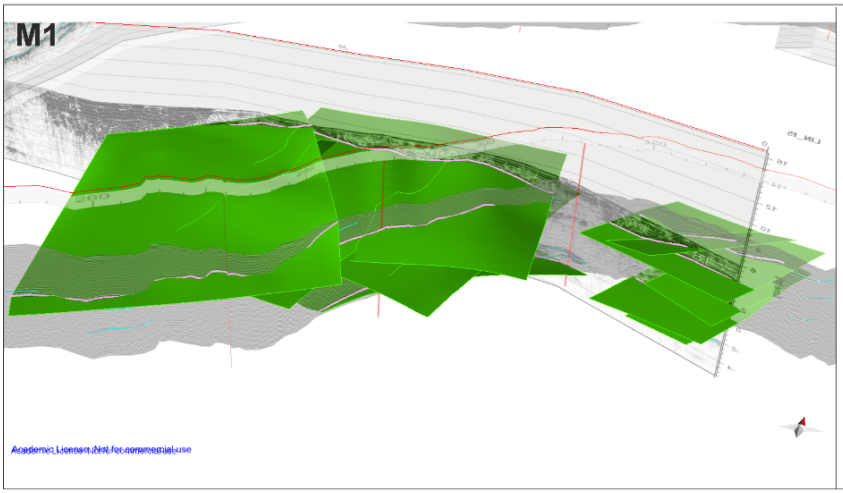

M1	Avg Dip	Avg Azm	Avg Str	A, m²
	2.8	181	91	1274
	15.9	288	198	81
	11.6	281	191	262
	11.3	112	22	595
	14	315	225	525
	14.3	333	243	111
	1.7	231	142	268
	7.1	174	84	119
	5.5	277	187	232
	8.4	254	164	106
	6.7	252	162	1316
	11.9	107	17	496

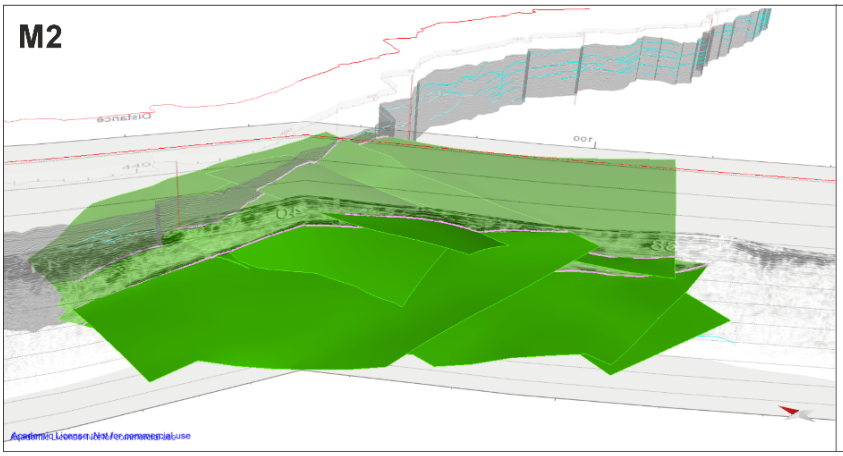

M2	Avg Dip	Avg Azm	Avg Str	A, m²
	7.3	249	158	1138
	27.7	229	139	48
	24.5	247	157	126
	18.3	240	150	83
	3.1	288	198	1125
	5.1	254	164	708
	8.7	271	181	1367
	7.5	257	167	394
	4.2	73	343	309

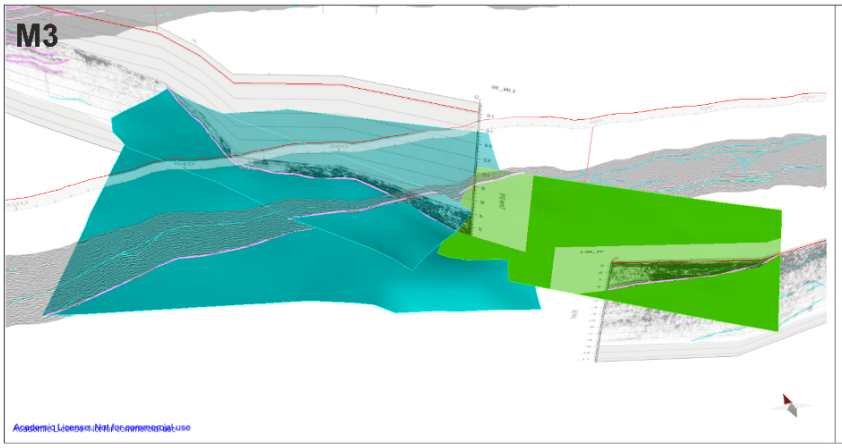

M3	Avg Dip	Avg Azm	Avg Str	A, m2
	6.3	209	119	3057
	8.4	167	77	946
	15.2	219	129	900

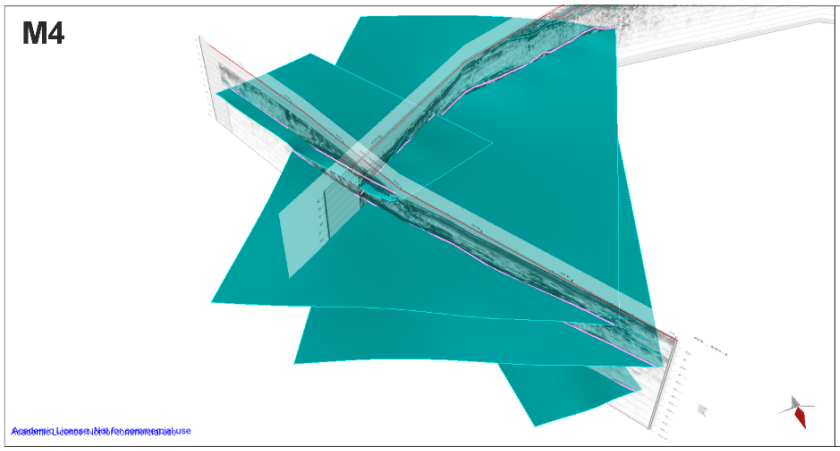

M4	Avg Dip	Avg Azm	Avg Str	A, m²
	6.1	149	59	2384
	7.6	154	64	2086
	3.1	169	79	464
	5.0	134	44	500

Fig 23. Middle clusters M1 – M4, their type (A or B, blue or green respectively) and statistical data on their dimensions

Southern area cluster

Only one cluster could be constructed on the southern side of the faults from the cutting point of L2 and L_S, making all the fractures in this cluster type A fractures (fig. 24). The largest fracture is situated right below surface level, with deeper lying fractures having significantly smaller surface areas. All except one of the fractures dip gently north, with the outlier having a roughly eastward dip.

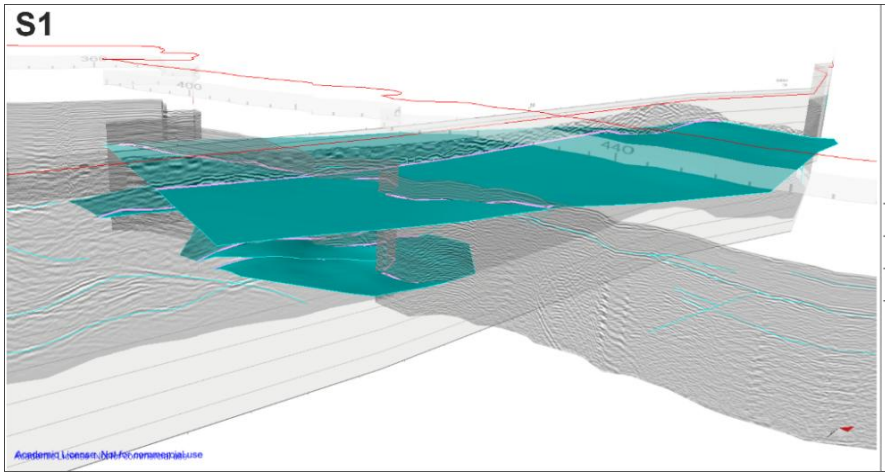

S1	Avg Dip	Avg Azm	Avg Str	A, m^2
	3.8	328	238	196
	3.0	3	273	182
	2.0	306	216	2220
	4.3	75	345	152

Fig 24. Southern cluster, all of which are type A, and statistical data.

4.4 Borehole R307 fracture surfaces

A total of 30 intersecting fracture traces were observed from the borehole GPR image and 26 of these intersecting fractures were able to be modelled into planar surfaces. 14 of these were located above the fault zone, 6 within the fault zone, and 6 below the fault zone. The diameters of these fractures vary between 8 - 33 m. The size distribution of fractures is rather constant, with the largest fractures (> 20 m diameter) being found in each interval (Bh1, Fz, Bh2), though the smaller fractures (< 20 m diameter) are found more frequently in the surface layers of Bh1. The relative amount of large fracture planes is thus bigger in Bh2 compared to Bh1 for example. The dip distribution does not appear diameter-dependent, with larger and smaller fractures having both gentler and steeper

dips. The largest apertures are found in the very surface layers in Bh1 and Fz, with considerably smaller apertures being hosted in Bh2.

In Bh1, most of the Set III fractures show no clear clustering, with a few Set I parallel fractures being present. In Fz, most of the fractures are part of Set I, which is also thought to represent the rough orientation of the fault. The singular outlier in Fz hosts a large aperture and it is part of the secondary fractures set constrained only within Fz (fig. 25). In Bh2, all fractures dip relatively shallow into the west and are considered to be part of Set III.

Table 2. Properties and the criteria for their selection. Ap = aperture size. For coloring scheme, see chapter 3.5.2

Dip	Dir	Str	Mes. Dpt.	Criteria	Ap (mm)	Diam. (m)	A (m^2)
16	132	42	9.3	Upper Broken zone, Ap:60mm	60	17	289
10	60	330	11.9	Second to lowest Broken zone Ap:20	20	10	100
12	341	251	14.1	Closest major frature Ap:5mm	5	10	100
8	81	351	18.2	Upper major fracture Ap:15mm	15	16	256
10	60	330	26.1	"Minor open" of the cluster Ap:1mm	1	8	64
25	159	69	36.4	Broken zone Ap:10mm	10	13	169
36	294	204	45.1	Largest aperture of the cluster	4	23	529
49	344	254	48.9	Largest aperture of the cluster Ap:2mm	2	10	100
30	321	231	59.4	Only one in the vicinity Ap:1mm	1	12	144
6	337	247	59.9	Only one in the vicinity Ap:1mm	1	11	121
88	172	82	62.5	Only one with aperture in cluster	5	12	144
18	266	176	72.3	Only aperture in vicinity Ap:5mm	5	22	484
64	176	86	86.7	"Minor farcture" Ap:5mm	5	11	121
75	170	80	87.4	"Partially open" Ap:3mm	3	9	81
70	140	50	99.2	Upper major Ap:15mm	15	9	81
65	166	76	101.8	Largest aperture Ap:19mm	19	22	484
46	234	144	108.2	Largest aperture Ap:5mm	5	25	625
48	131	41	125	Upper major fracture Ap:14mm	14	14	196
64	168	78	126.1	"Minor open" Ap:4mm	4	26	676
80	175	85	132.9	131.2 weathered bedrock. Taken from nearest measurements	1	19	361
23	262	172	148.6	Nearest in vicinity Ap:1mm	1	8	64
13	269	179	149.2	Nearest in vicinity Ap:1mm	1	24	576
27	289	199	164.9	Nearest in vicinity Ap:1mm	1	27	729

22	301	211	169.9	Nearest in vicinity Ap:2mm	2	9	81
15	312	222	173	Upper open based on ABI Ap:0mm	0	33	1089
19	221	131	184.4	Nearest in vicinity Ap:0mm	0	9	81

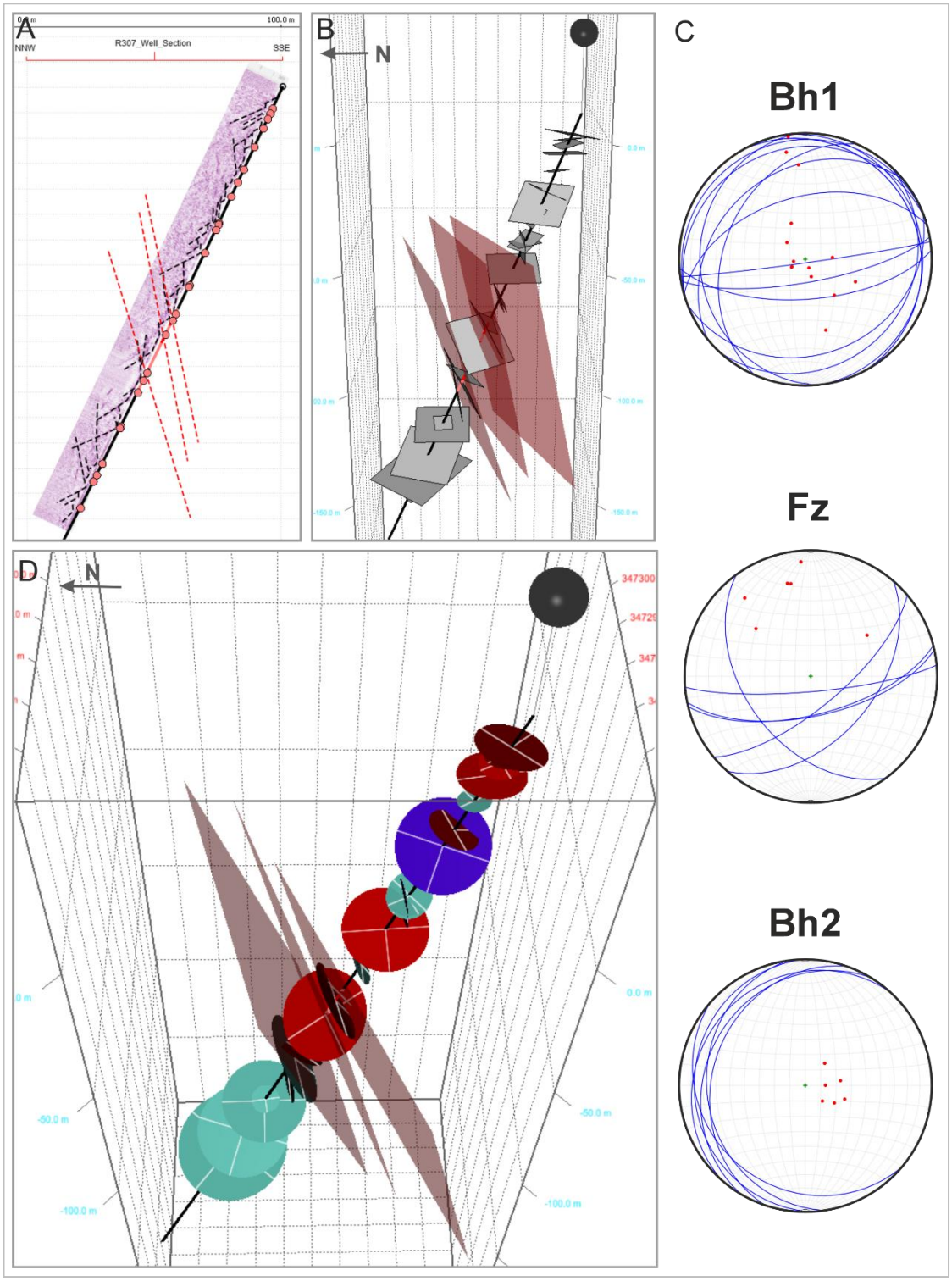

Fig 25. A: cross-section view of the BHGPR image with fracture traces (dashed black lines), intersection points (beige points) and projected fault planes (dashed red lines) visible. B:

generated fractures presented as MOVE *fracture set*. C: Stereoplots of constructed fracture planes within Bh1, Fz, Bh2. D: fracture set presented as a *dip data*. For coloring scheme, see chapter 3.5.2

5 Discussion

The faults, field-measured fractures, horizontal GPR fractures, and borehole fractures were compiled into a 3D model (presented in fig. 26). Due to the difficulties in observing the nature of horizontal fracturing, it is often excluded from 3D models. The focus here was placed upon detecting and determining the geometry of these fractures, for which these methods proved to be sufficient. An overview and interpretations of the model are presented below, followed by a discussion of the methodology.

5.1 Structural 3D model and geological interpretations

The aeromagnetic signals were interpreted to represent the general trends of the geologic structures in the area. The study area lies between the NW and NE trending magnetic signals, within a patch of E-W trending anomaly, which are parallel to JSZ, PMSZ and SFSZ, respectively. The “cup” shape of the trends is thought to be connected to the movement of the proximal shear zones (described in chapter 2.3), namely the SFSZ and PMSZ, with the JSZ considered to have less of an impact because of its more distal location. These signals are roughly consistent with the foliation observations in Nordbäck et al. (2023, fig. 6) and the trend of the local lineament set, as well as field fracture Set I. In addition, the larger northern- and southern faults are also concurrent with the aeromagnetic trends, foliation, local lineament trend and Set I. Thus, Set I and at least the northern and southern faults are considered to have formed following the precursors formed by earlier ductile deformation. The faults are also likely to have been reactivated at some point during the multiple brittle reactivation events (described in Mattila and Viola, 2014).

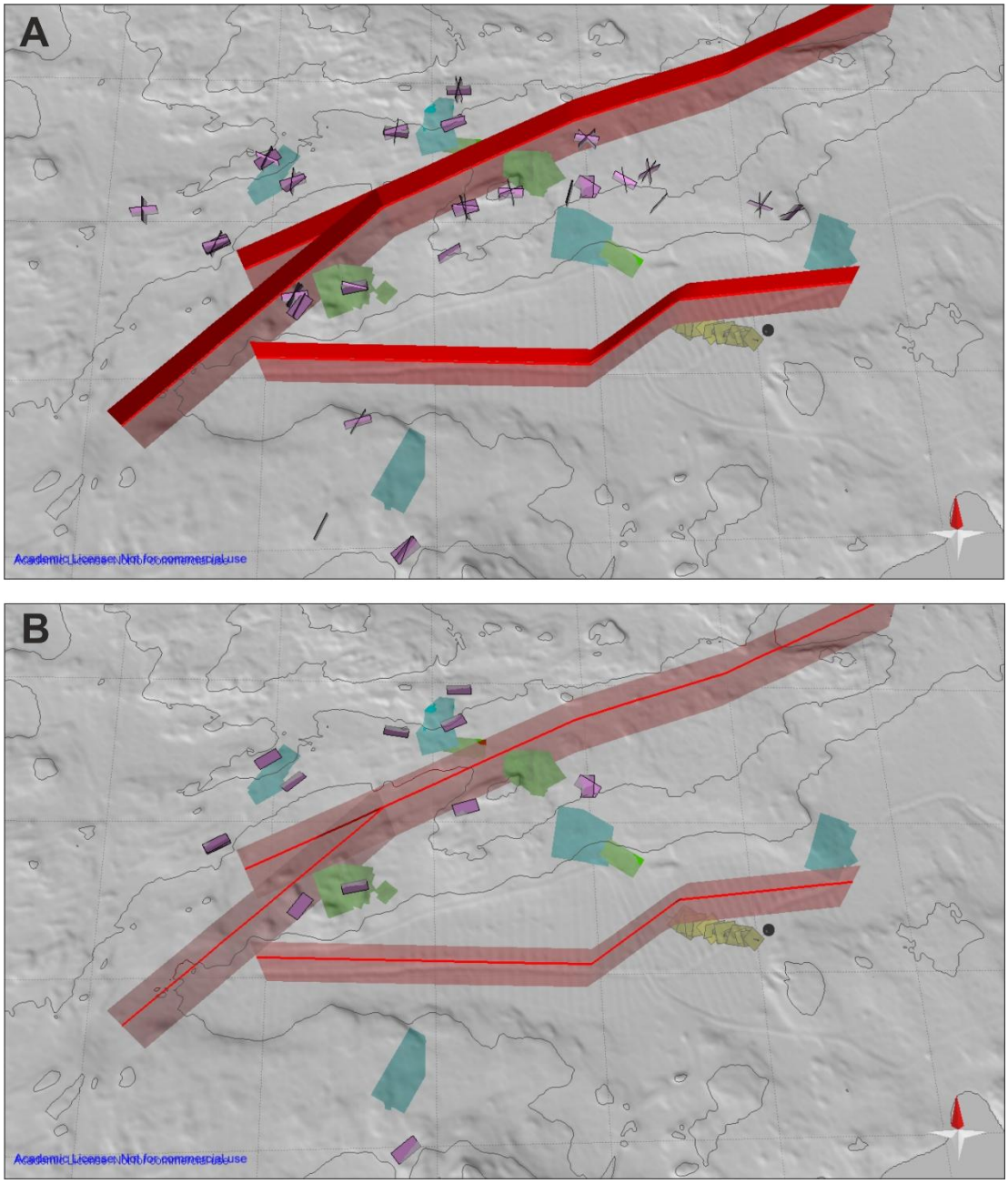

Fig 26. A: complete 3D model, B: Horizontal structures of the 3D model. Red planes=faults, green and blue planes=surface GPR modelled fracture planes, yellow planes=BHGPR modelled fracture planes and pink planes=extruded planes of field measurements.

The ERT works best in areas with little to no soil cover (Huotari and Wennerström, 2017) and it is not possible to derive orientational attributes from it. Thus, the wider sediment filled depression of the southern fault casts some uncertainties on the exact geometry of the fault plane, since the only concrete orientational data is available from a single borehole. The wider depression is most likely formed due to enhanced glacial erosion that can be driven by larger damage zones or favorable orientations of large brittle structures (Skyttä et al., 2023). Fossen (2010) presented a largening damage zone to be possible in

cases where the fault plane bends, or where multiple fault planes are oriented in a step pattern and connected by increased fracturing. The most confident geometry is thought to be achieved for the northern fault, due to the pronounced topographical depression, it being visible in both ERT and surface GPR, as well as the direct structural measurements taken from the wall. The extent of the western fault is fairly reliably quantified from the surface GPR and DEM, but the orientation could only be inferred from proximal field measurements. Its presence is also not prominent in the ERT data.

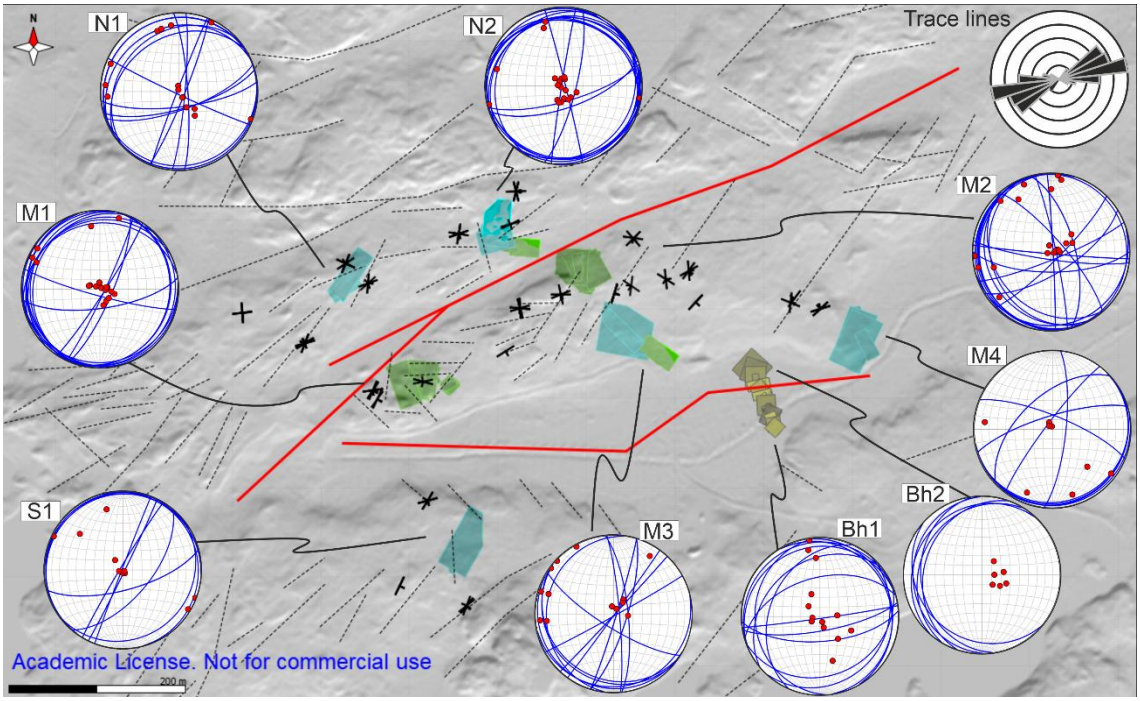

Fig 27. Compiled stereoplots of field measurements and modelled planes divided into clusters described in chapter 4.3. Rose plot represents the orientations of local lineaments.

Measurements interpreted as Set I show more orientational variation than Set II as the strikes of Set II seem quite uniform (stereograms of figs. 19 and 27). Set II is more prominent near and between the faults compared to the entire study area (chapter 4.1) and though the traces of the local lineaments are parallel with Set I measurements for the most part, they seem to adhere to Set II measurements in some localities (fig. 27). Field measurements of M4 appear as trend outliers, where some familiar strike directions are observed but dip directions are opposite. The diabase dikes of Kopparnäs that intruded in E-W dextral dilations and later into N-S striking sinistral dilations that crosscut the older structures (Pajunen et al., 2008; Sakaguchi, 2017). Both sets of dikes are linked with the reactivations of E-W and N-S trending shear/fault zones in a SE-NW transpression

environment (Pajunen et al., 2008). The relationship of these dike intruded structures, and their previously determined genesis process indicates a similar relationship and formation process for the correspondingly oriented Set I and Set II, though further work focusing on this aspect would need to be done in order to draw any conclusions. Fractures with similar characteristics to that of Set II have been interpreted to be due to brittle faulting in Ruuska et al. (2025), for instance, but the sharp changes in ductile foliation trends presented in Nordbäck et al. (2023) and limited foliation observations cause some doubt on similar interpretations here. Joint Sets I and II were thus visualized with the same objects, since no concrete differentiation could be done according to hierarchy, age, clear orientational trends, or consistent link with local lineament trends around the fracture clusters.

Surface GPR fracture clusters in the immediate vicinity of fault planes (namely N2, M1, M2) host more fracture planes as well as intricate and complex fracture systems compared to the ones further away. This is interpreted to be due to the increased anisotropy near the faults (Skyttä et al., 2021), however, if this fracturing is directly linked with the fault remains unclear. It's important to note that these clusters consist mainly of type B planes, so these differences could be methodology-related as well.

Only Set I and Set III fracturing are present in the fracture set produced from the R307, while Set II is completely absent. This is likely due to R307 being oriented parallel to Set II strikes, which prevents fracture planes from intersecting the borehole and being present in the OBI/ABI images. The horizontal fracturing observed from the borehole surface layers shows more sporadic orientation than the surface GPR modelled fractures as the latter presents some clustering of dip directions and/or dip values, though not enough to be discerned as separate fracture sets. In addition, R307 fractures host somewhat steeper dips of Set III fractures. Direct correlation of Bh1 horizontal fracture extents and orientations with surface GPR results proved difficult, for R307 is located quite far from cluster S1 and separated by SF from M4. Fractures in the more proximal M4 cluster into a SE-directed dip, whereas the Bh2 fractures cluster into a W directed dip, showing larger differences of dip directions than between the proximal M3 and M4 for example. The location of the Bh2 W dipping fractures near the fault core and at greater depths is thought to play a major part here.

5.2 2D GPR and BHGPR images

The surface GPR was successful at imaging air- or water-filled horizontal to subhorizontal fractures in the subsurface similar to Molron et al. (2020) and Porsani et al. (2006), for instance. Tests by Song et al. (2025) demonstrated that larger fractures near the surface may obscure interpretations of deeper lying discontinuities, however the reflectors and their sizes appear to be quite evenly distributed in depth, so no major systematic errors are thought to have occurred here. Molron et al. (2020) concluded that the GPR is able to image the most permeable subhorizontal structures in low permeability environments, with 80 % of open fractures dipping 0 - 25° being imaged. However, this number dropped to 42 % when considering also the closed subhorizontal fractures and to 5.5 % when considering all fractures regardless of orientation or aperture. This conclusion is concordant with the results in this study, as the vast majority of modelled fractures host subhorizontal dips and appear as very high-contrast reflections in GPR images. Some fractures with dips over 25° are observed, and there is a clear absence of subvertical to vertical fracture traces. Multiple alternative methods exist for mapping and characterizing vertical fractures such as 3D photogrammetry and fracture tracing using drone ortophotos (Smeraglia et al. 2021; Nordbäck et al. 2023 respectively). Additional field mapping could be done to assess supplemental attributes, such as aperture sizes and hierarchies.

In surface GPR, horizontal fracturing can be observed to be somewhat denser in areas proximal to fault zones, often dipping towards the fault. The trend is not as clearly visible in the BHGPR image, which can be partly explained by the harder-to-interpret nature of the BHGPR images. The fracturing intensity in R307 is well-constrained in the data derived from OBI/ABI, since the fractures are clearly visible in the images. A high fracture density is observed in the surface layer followed by a significant decrease from 20 to 90m. A second high intensity zone is encountered within the fault zone, followed again by a sharp decrease below the fault (fig. 28). Only the increased fracturing of the surface layer is observable in the BHGPR-derived fracture set and the general fracture intensity is considerably lower. The reason for these discrepancies between BHGPR interpreted fractures and numerical fracture data is likely due to the “oversaturation” of fractures resulting in abundance of pore water and high amounts of wave scattering that disrupts imaging of individual fractures (Dorn, 2013; Walton et al., 2015). A similar effect is seen with the surface GPR over the fault zones, but not necessarily in the general surface layer fracturing. The clearer to interpret image of the surface GPR could be due

to the smaller dip range observed (0-25° in surface GPR, Molron et al., 2020 and 30 – 90° in BHGPR, Dorn et al., 2012), making the increased censoring in surface GPR actually beneficial for imaging discrete fractures.

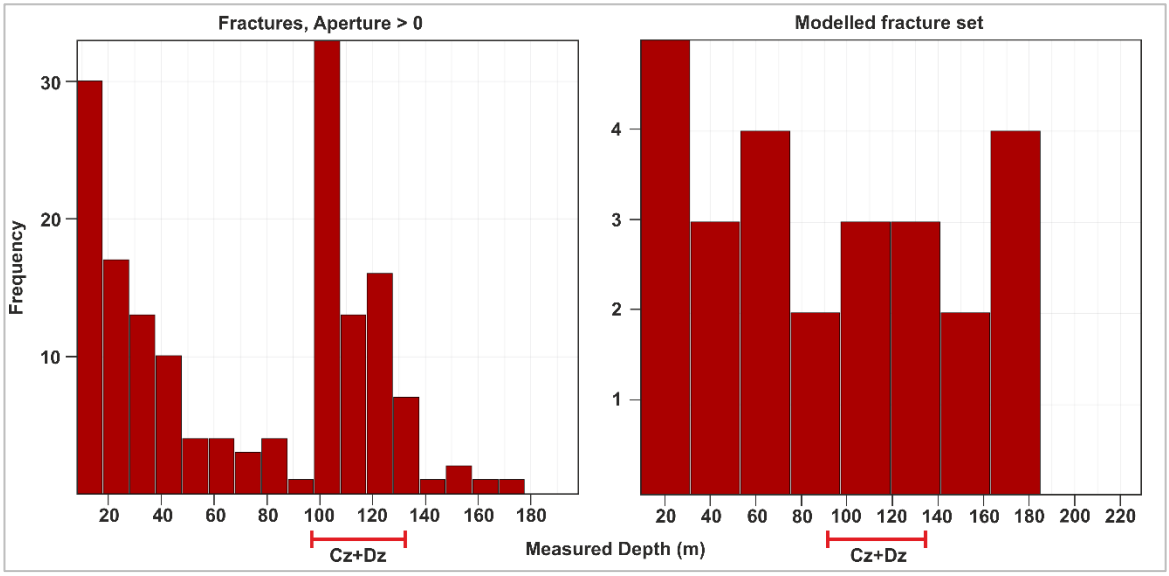

Fig 28. Differences in fracturing intensity between open fractures observed in OBI/ABI (left) and BHGPR derived fracture set (right).

The results in Olsson et al. (1992), Dorn et al. (2012), and Serzu et al. (2004) show that BHGPR is adequate for detecting discrete water-saturated fractures with high depth penetration. The uncertainty in the borehole workflow in this study comes mainly from linking OBI/ABI-determined fractures and BHGPR-derived fracture traces. Dorne et al. (2012) found it feasible to correlate BHGPR imaged reflectors to conductive fractures interpreted previously from televiewer data (among other methods, see Le Borgne et al. (2007) for comprehensive list). In addition, Olsson et al. (1992) noticed that the groundwater flow is controlled by a few major fractures. Given that the major fractures are most robustly imaged in BHGPR, are most prominent in OBI/ABI images and are relatively scarce, it can be reasonably assumed that these fractures are well-constrained using the methods in this study. By extension, the directional and dimensional properties of these conductive fractures are well-constrained. Conversely, the lower one goes in fracture hierarchy, the more the uncertainties are thought to grow and it is also possible for reflectors to appear that are not interpreted as open fractures in televiewer data (Dorn et al., 2012). It is noteworthy that because BHGPR takes images without discretion for

dip direction, another censoring criterion is encountered in angled boreholes. Fractures with certain combinations of dip and dip direction cannot be imaged even though the dip value corresponds to the observed limit of 90-30° in relation to the borehole.

5.3 3D fracture surfaces

Both parallel-, and crosscutting GPR lines have been used to model 3D surfaces (Meschede et al., 1997; Christie et al., 2009; Markovaara-Koivisto, 2017; Molron et al., 2020). In this study, more definite dimensional and orientational properties are thought to have been achieved for type A fracture planes since the "skeleton" determines both parameters well. In the fractured bedrock such as that of Kopparnäs, the truncation of these horizontal fractures could cast uncertainty on the symmetrical dimensions, since it is possible that vertical fractures abut horizontal ones.

For type B planes, the closer the survey lines are, the easier the trace linking gets, but the dimensions must be extrapolated further. One way to systematically unify results would be to adopt certain aspect ratios for modelling dimensions. Since extensional fractures ideally develop as ellipses (Fossen, 2016), 2:1 aspect ratio could be used for example. In this case, the short or long axis would be imaged in GPR and if the parallel line's trace is further than twice the trace length's distance away, it would not be considered. On the other hand, this would set a predetermined amount of surface extrapolation for uncertain dimensions based on observed properties. This system could also be used to plan the number of crosscutting GPR survey lines that is adequate, and how close the crossing points should be to each other. For example, fewer longer lines could run along the long axis of a fracture with multiple shorter ones running across, parallel to the short axis. Similar ratios could be adopted for the BHGPR fracture surfaces though deciding whether the long or short axis is imaged would be harder.

DFN modelling is a commonly used method for analysing fracture network properties (in Romano et al. 2020; Smeraglia et al. 2021, for instance). DFN models present geometrical properties of fractures such as orientations, sizes, shapes, apertures, curvature, as well as topological relationships of individual fractures and fracture sets (Lei et al., 2017). For fracture planes modelled in this study, detailed topological analysis cannot be done directly but some assessments can be made on for example which fractures are connected,

and which are not. This is more intuitive in surface GPR, where true traces are readily visible, and it requires more concern in BHGPR where fracture traces are presented as two tails. In addition, attributes like fracture curvature are easier to determine in surface GPR compared to the BHGPR (surface GPR in Saksa et al., 2005 and BHGPR curvature in Escallon et al., 2024). For BHGPR Sanderson and Nixon 2015) shows the possibility to assess topology using crosscutting relationships visible in OBI/ABI images. Another method could be to use the multi-hole approach mentioned by Dorn et al. (2012), in which three-dimensional relationships of fractures could be determined from boreholes situated in a triangular pattern. For surface GPR fractures and upright fractures, the assessment of relationships is not straightforward either, but field assessments of topology between delineated fracture sets could provide more accurate approximations for further modelling.

In essence, using multiple methods to target different aspects or geological structures would have the best chance to comprehensively quantify fracture systems by utilizing the strengths of each method. For future work, surface GPR methods could be used to model often-excluded horizontal fractures, and vertical fractures could be characterized using established remote sensing and field mapping methods. The depth distribution of hydraulically conductive fractures could be enhanced with BHGPR, while possibly increasing the resolution for surface layer observations. In the best-case scenario, the borehole from which this is conducted would be as close as possible, though drilling new boreholes may not always be financially feasible. The coupled results could then be presented as a block model hosting a deterministically defined fracture system and conducting multiple of these “blocks” could possibly be used to calculate bulk flow models of an area.

6 Conclusions

In this study, the joint use geophysical methods (GPR, ERT and BHGPR) along with field data has proven sufficient for i) modelling approximations of fault plane geometries ii) identifying and imaging horizontal fractures in homogenous surface layer bedrock, iii) 3D modelling horizontal fracture surfaces with quantified geometries (dimensions and orientations), iv) imaging strongly reflecting discrete fractures and fracture zones in depth

and v) determining the geometries of these fractures and modelling them as 3D surfaces. This study is meant to act as base data for further work in the area, such as DFN and fluid flow modelling.

The three main faults were interpreted to have been formed along ductile deformation precursors, and the study area was interpreted to be dominated by E-W and N-S striking upright fracture sets. Abundant horizontal fracturing was observed in the surface GPR and from field data that was considered to have formed due to deglaciation-induced uplift.

The surface GPR was able to image non-outcropping fractures, and crosscutting surveys were found to be optimal for modelling fracture planes. In total, 626 horizontal to subhorizontal fracture traces were identified, 113 of which were used in fracture plane construction. 47 planes were constructed hosting extents between 29 m^2 and 3060 m^2 and dips between 1° and 27.7°, with most dips being under 20°. BHGPR was found to be suited to image highly reflective fractures and provide data on their dimensions. A total of 30 intersecting conductive fractures were interpreted, 26 of which were modelled into fracture planes. These planes had diameters ranging from 8 m to 33 m and areas between 64 m^2 and 1089 m^2. Dips of these planes follow the main clustering of numerical fracture data.

To conclude, the surface GPR can be used as a mapping tool for horizontal fractures as well as a tool for determining their geometrical attributes, whereas BHGPR is more of an assessment tool for discrete hydraulically conductive fractures. The compiled structural 3D model consists of i) three extruded fault planes, ii) seven clusters of geometrically constrained horizontal fracture planes derived from surface GPR, iii) a set of field measurement-derived mesh planes representing upright fractures around the horizontal fracture clusters, and iv) a fracture set derived from borehole R307.

Acknowledgements

First and foremost, I would like to thank my supervisors Eemi Ruuska from the University of Turku and Jon Engström from GTK for the opportunity to do this thesis as well as their supervision and guidance during this process. In addition, I'd like to thank Petri Valasti and Mira Markovaara-Koivisto from GTK for their work regarding the surface GPR data acquisition and processing as well as their help with data interpretation. I thank Alexis Shakas from ETH Zurich for his help in acquiring, interpreting and understanding the BHGPR data. I thank my family, fellow students and my spouse Elisa for their continued support through this process. Lastly, I would like to thank the geohouse coffee machine for providing me with liquid motivation.

References

Aizebeokhai, A.P. and Oyeyemi, K.D. 2014. The use of the multiple-gradient array for geoelectrical resistivity and induced polarization imaging. *Journal of Applied Geophysics* 111, pp. 364–376. doi: 10.1016/j.jappgeo.2014.10.023.

Annan, A.P. 2003. *Ground Penetrating Radar Principles, Procedures & Applications*. Mississauga: Sensors & Softwares Incorporated. 278p.

Annan, A.P. 2008. Electromagnetic Principles of Ground Penetrating Radar. In: *Ground Penetrating Radar Theory and Applications*. Elsevier, pp. 1–40. doi: 10.1016/B978-0-444-53348-7.00001-6.

Le Borgne, T., Bour, O., Riley, M., Gouze, P., Pezard, P., Belghould, A., Lods, G., Le Provost, R., Greswell, R., Ellis, P., Isakov, E. and Last, B. 2007. Comparison of alternative methodologies for identifying and characterizing preferential flow paths in heterogeneous aquifers. *Journal of Hydrology* 345(3–4), pp. 134–148. doi: 10.1016/j.jhydrol.2007.07.007.

Bossennec, C., Frey, M., Seib, L., Bär, K. and Sass, I. 2021. Multiscale characterisation of fracture patterns of a crystalline reservoir analogue. *Geosciences* 11(9), p. 1. doi: 10.3390/geosciences11090371.

Caine, J.S., Evans, J.P. and Forster, C.B. 1996. Fault zone architecture and permeability structure. *Geology* 24(11), pp. 1025–1028. doi: 10.1130/0091-7613(1996)024<1025:FZAAPS>2.3.CO;2.

Chabani, A., Trullenque, G., Ledésert, B.A. and Klee, J. 2021. Multiscale characterization of fracture patterns: A case study of the noble hills range (Death Valley, CA, Usa), application to geothermal reservoirs. *Geosciences* 11(7), pp. 1–28. doi: 10.3390/geosciences11070280.

Christie, M., Tsoflias, G.P., Stockli, D.F. and Black, R. 2009. Assessing fault displacement and off-fault deformation in an extensional tectonic setting using

3-D ground-penetrating radar imaging. *Journal of Applied Geophysics* 68(1), pp. 9–16. doi: 10.1016/j.jappgeo.2008.10.013.

Davy, P., Bour, O., De Dreuzy, J.R. and Darcel, C. 2006. Flow in multiscale fractal fracture networks. *Geological Society Special Publication* 261, pp. 31–45. doi: 10.1144/GSL.SP.2006.261.01.03.

Dorn, C. 2013. *Fracture Network Characterization using Hydrological and Geophysical Data*. Doctoral Dissertation, Lausanne: Universit´e de Lausanne. Available at: https://hal.science/tel-01099410v1.

Dorn, C., Linde, N., Borgne, T. Le, Bour, O. and de Dreuzy, J.R. 2013. Conditioning of stochastic 3-D fracture networks to hydrological and geophysical data. *Advances in Water Resources* 62(PA), pp. 79–89. doi: 10.1016/j.advwatres.2013.10.005.

Dorn, C., Linde, N., Doetsch, J., Le Borgne, T. and Bour, O. 2012. Fracture imaging within a granitic rock aquifer using multiple-offset single-hole and cross-hole GPR reflection data. *Journal of Applied Geophysics* 78, pp. 123–132. doi: 10.1016/j.jappgeo.2011.01.010.

Ehlers, C., Lindroos, A. and Selonen, O. 1993. The late Svecofennian granite-migmatite zone of southern Finland – a belt of transpressive deformation and granite emplacement. *Precambrian Research* 64(1), pp. 295–309.

Elminen, T., Airo, M.-L., Niemelä, R., Pajunen, M., Vaarma, M., Wasenius, P. and Wennerström, M. 2008. Fault structures in the Helsinki area, southern Finland. *Geological Survey of Finland, Special Paper* 47, pp. 185–213.

Elminen, T., Airo, M.-L., Niemelä, R., Pajunen, M., Wasenius, P. and Wennerström, M. 2006. Extensional brittle structures and their relations to the bimodal 1.6 Ga magmatism in the Helsinki region, southern Finland. *Bulletin of the Geological Society Finland, Special Issue* 1, p. 31.

Elming, S.-Å. and Mattsson, H. 2001. Post Jotnian basic Intrusions in the Fennoscandian Shield, and the breakup of Baltica from Laurentia: a palaeomagnetic and AMS study. *Precambrian Research* 108, pp. 215–236. Available at: www.elsevier.com/locate/precamres.

Engström, J., Markovaara-Koivisto, M., Ovaskainen, N., Nordbäck, N., Paananen, M., Aaltonen, I., Martinkauppi, A., Laxström, H. and Wik, H. 2025. Mapping of lineaments in Finland at the scale of 1:500 000. *Norwegian Journal of Geology* 105(1), pp. 1–21. Available at: https://njg.geologi.no/publications/mapping-of-lineaments-in-finland-at-the-scale-of-1500-000/.

Engström, J., Bischoff, A., Kortunov, E., Markovaara-Koivisto, M., Ovaskainen, N., Nordbäck, N. and Paananen, M. 2024. Structural, petrophysical, and geophysical characterization of a fault zone in southern Finland - application for subsurface fluid flow in granitic settings. *EGU General Assembly 2024, Vienna, Austria,* , pp. 14–19. doi: 10.5194/egusphere-egu24-6192.

Escallon, D., Shakas, A. and Maurer, H. 2024. Modelling and inferring fracture curvature from borehole GPR data: A case study from the Bedretto Laboratory, Switzerland. *Near Surface Geophysics* 22(2), pp. 235–254. doi: 10.1002/nsg.12286.

Faulkner, D.R., Jackson, C.A.L., Lunn, R.J., Schlische, R.W., Shipton, Z.K., Wibberley, C.A.J. and Withjack, M.O. 2010. A review of recent developments concerning the structure, mechanics and fluid flow properties of fault zones. *Journal of Structural Geology* 32(11), pp. 1557–1575. doi: 10.1016/j.jsg.2010.06.009.

Fossen, H. 2010. *Structural geology*. Cambridge: Cambridge University Press. 463p.

Frey, M., Bossennec, C., Seib, L., Bär, K. and Sass, I. 2021. Interdisciplinary Fracture Network Characterization in the Crystalline Basement: A case study from the Southern Odenwald, SW Germany. *Solid Earth* 13. Available at: https://se.copernicus.org/articles/13/935/2022/se-13-935-2022-discussion.html.

Frey, M., Bossennec, C., Seib, L., Bär, K., Schill, E. and Sass, I. 2022. Interdisciplinary fracture network characterization in the crystalline basement: a case study from the Southern Odenwald, SW Germany. *Solid Earth* 13(6), pp. 935–955. doi: 10.5194/se-13-935-2022.

Geologian Tutkimuskeskus (GTK). 2016. *Lentogeofysikaalinen magneettinen anomaliakartta*. Available at: https://hakku.gtk.fi/fi/locations?orderBy=nameFi&search=aeromagneetti&submit=true [Accessed: 8 April 2025].

Geologian Tutkimuskeskus (GTK). 2022. *Kallioperä 200k*. Available at: https://hakku.gtk.fi/fi/locations?orderBy=nameFi&search=fault&submit=true [Accessed: 8 April 2025].

Gorbatschev, R. and Bogdanova, S. 1993. Frontiers in the Baltic Shield. *Precambrian Research* 64, pp. 3–21.

Hartley, L., Appleyard, P., Baxter, S., Hoek, J., Joyce, S., Mosley, K., Williams, T., Fox, A., Cottrell, M., La Pointe, P., Gehör, S., Darcle, C., Le Goc, R., Aaltonen, I., Vanhanarkaus, O., Löfman, J. and Poteri, A. 2018. Discrete Fracture Network Modelling (Version 3) in Support of Olkiluoto Site Description 2018. *Posiva Working Report* 2017–32, 820p.

Hasan, M., Shang, Y. and Jin, W. 2018. Delineation of weathered/fracture zones for aquifer potential using an integrated geophysical approach: A case study from South China. *Journal of Applied Geophysics* 157, pp. 47–60. doi: 10.1016/j.jappgeo.2018.06.017.

Hasan, M., Shang, Y., Meng, H., Shao, P. and Yi, X. 2021. Application of electrical resistivity tomography (ERT) for rock mass quality evaluation. *Scientific Reports* 11(1), pp. 1–19. doi: 10.1038/s41598-021-03217-8.

Heeremans, M. and Wijbrans, J. 1999. Late Proterozoic tectonic events in southern Finland, constrained by 40 Ar/ 39 Ar incremental heating and single spot fusion experiments on K-feldspars. *Terra Nova* 11, pp. 216–222.

Hölttä, P. and Heilimo, E. 2017. Metamorphic Map of Finland. *Special Paper - Geological Survey of Finland* 60, pp. 75–126.

Huhma, H. 1986. *Sm-Nd, U-Pb and Pb-Pb isotopic evidence for the origin of the Early Proterozoic Svecokarelian crust in Finland*. Geologian tutkimuskeskus ; Available from Govt. Print. Centre.

Huotari, T. and Wennerström, M. 2017. Integroitujen geofysikaalisten ja kallioperägeologisten tutkimusmenetelmien kehittäminen

yhdyskuntarakentamisen tarpeisiin. *Geologian Tutkimuskeskus Tutkimusraportti* 231, 140p.

Kähkönen, Y. 2005. Svecofennian supracrustal rocks. In: *Precambrian Geology of Finland - Key to the Evolution of the Fennoscandian Shield*. Amsterdam: Elsevier B.V., pp. 343–406.

Kara, J. 2021. *Evolution of the Svecofennian bedrock in Southern Finland - Spatial and temporal changes in the mantle-derived magmatism and mantle-crust interaction*. Doctoral Dissertation, University of Turku.

Kara, J., Väisänen, M., Johansson, Lahaye, Y., O'Brien, H. and Eklund, O. 2018. 1.90-1.88Ga arc magmatism of central fennoscandia: Geochemistry, U-Pb geochronology, Sm-Nd and lu-hf isotope systematics of plutonic-volcanic rocks from southern Finland. *Geologica Acta* 16(1), pp. 1–23. doi: 10.1344/GeologicaActa2018.16.1.1.

Kauti, T. 2016. *Salon seudun kallioperän alueellinen 3D-malli-rakenteiden kontrollina duktiilit hiertovyöhykkeet ja Svekobaltinen transpressio*. Master's Thesis, Turun Yliopisto.

Korja, A., Korja, T., Luosto, U. and Heikkinen, P. 1993. Seismic and geoelectric evidence for collisional and extensional events in the Fennoscandian Shield-implications for Precambrian crustal evolution. *Tectonophyscs* 219, pp. 129–152.

Korsman, K., Korja, T., Pajunen, M., Virransalo, P., Ekhdal, E., Elo, S., Haapala, I., Heikkinen, P., Hjelt, S., Hölttä, P., Huhma, H., Idman, H., Jokinen, J., Kähkönen, Y., Kilpeläinen, T., Koistinen, T., Komminaho, K., Kontinen, A., Korhonen, J., Korja, A., Kousa, J., Kukkonen, I., Kurimo, M., Lahtinen, R., Leino, M., Lerssi, J., Lindkvist, K., Lukkarinen, H., Luosto, U., Luukas, J., Luukkonen, E., Malaska, J., Mertanen, S., Niemelä, R., Nironen, M., Paavola, J., Papunen, H., Peltonen, P., Pesonen, L., Pietikäinen, K., Pihlaja, P., Rämö, T., Rastas, J., Ruotoistenmäki, T., Säävuori, H., Tervo, T., Tuisku, P., Vaasjoki, M., Väisänen, M., Wasenius, P. and Yliniemi, J. 1999. The GGT/SVEKA Transect: Structure and evolution of the continental crust in the Paleoproterozoic Svecofennian orogen in Finland. *International Geology Review* 41(4), pp. 287–333. doi: 10.1080/00206819909465144.

Kosunen, P. 1999. The Rapakivi Granite Plutons of Bodom and Obbnäs, Southern Finland; Petrography and Geochemistry. *Bulletin of the Geological Society of Finland* 71(2), pp. 275–304.

Lahtinen, R. 1994. Crustal evolution of the Svecofennian and Karelian domains during 2.1-1.79 Ga, with special emphasis on the geochemistry and origin of 1.93-1.91 Ga gneissic tonalites and associated supracrustal rocks in the Rautalampi area, central Finland. *Geological Survey of Finland, Bulletin* 378, p. 128.

Lahtinen, R., Korja, A. and Nironen, M. 2005. Paleoproterozoic Tectonic Evolution. In: *Precambrian Geology of Finland- Key to the Evolution of the Fennoscandian Shield*. Amsterdam: Elsevier B.V., pp. 482–532.

Laitala, M. 1961. *Pre-Quaternary Rocks of the Siuntio Map-Sheet area. Geological Map of Finland 1:100 000, Explanation to the Maps of Pre-Quaternery Rocks, Sheet 2032.*

Leckenby, R.J., Sanderson, D.J. and Lonergan, L. 2005. Estimating flow heterogeneity in natural fracture systems. *Journal of Volcanology and Geothermal Research* 148(1–2), pp. 116–129. doi: 10.1016/j.jvolgeores.2005.03.017.

Lei, Q., Latham, J.P. and Tsang, C.F. 2017. The use of discrete fracture networks for modelling coupled geomechanical and hydrological behaviour of fractured rocks. *Computers and Geotechnics* 85, pp. 151–176. doi: 10.1016/j.compgeo.2016.12.024.

Loke, M.H. 2022. Tutorial : 2-D and 3-D electrical imaging surveys. 194p. Available at: www.geotomosoft.com.

Luukas, J., Kousa, J., Nironen, M. and Vuollo, J. 2017. Major stratigraphic units in the bedrock of Finland, and an approach to tectonostratigraphic division. *Geological Survey of Finland, Special Paper* 60, pp. 9–40.

Maanmittauslaitos (MLL). 2022. *Korkeusmalli 2m*. Available at: https://www.maanmittauslaitos.fi/kartat-ja-paikkatieto/aineistot-ja-rajapinnat/tuotekuvaukset/korkeusmalli-2-m [Accessed: 8 April 2025].

Markovaara-Koivisto, M. 2017. *Visualization and modelling of rock fractures and rock quality parameters in 1- 3 dimensions in crystalline bedrock*. Doctoral Dissertation, Aalto University. Available at: http://urn.fi/URN:ISBN :978-952-60-7754- 3.

Markovaara-Koivisto, M., Hokkanen, T. and Huuskonen-Snicker, E. 2014. The effect of fracture aperture and filling material on GPR signal. *Bulletin of Engineering Geology and the Environment* 73(3), pp. 815–823. doi: 10.1007/s10064-013-0566-4.

Mattila, J. and Viola, G. 2014. New constraints on 1.7Gyr of brittle tectonic evolution in southwestern Finland derived from a structural study at the site of a potential nuclear waste repository (Olkiluoto Island). *Journal of Structural Geology* 67(PA), pp. 50–74. Available at: http://dx.doi.org/10.1016/j.jsg.2014.07.003.

Meschede, M., Asprion, U. and Reicherter, K. 1997. Visualization of tectonic structures in shallow-depth high-resolution ground-penetrating radar (GPR) profiles. *Terra Nova* 9(4), pp. 167–170. doi: 10.1046/j.1365-3121.1997.d01-25.x.

Middleton, M., Schnur, T., Sorjonen-Ward, P. and Hyvönen, E. 2015. Geological Lineament Interpretation Using The Object-Based Image Analysis Approach: Results of Semi-Automated Analyses Versus Visual Interpretation. *Geological Survey of Finland, Special Paper* 57, pp. 135–154.

Milsom, J. 2003. *Field Geophysics*. Third Edition. Chichester: John Wiley & Sons Ltd. 223p.

Molron, J., Linde, N., Baron, L., Selroos, J.O., Darcel, C. and Davy, P. 2020. Which fractures are imaged with Ground Penetrating Radar? Results from an experiment in the Äspö Hardrock Laboratory, Sweden. *Engineering Geology* 273, pp. 1–21. doi: 10.1016/j.enggeo.2020.105674.

Mörner, N.A. 1978. Faulting, fracturing, and seismicity as functions of glacio-isostasy in Fennoscandia. *Geology* 6(1), pp. 41–45. doi: 10.1130/0091-7613(1978)6<41:FFASAF>2.0.CO;2.

Niculescu, B.M. and Andrei, G. 2021. Application of electrical resistivity tomography for imaging seawater intrusion in a coastal aquifer. *Acta Geophysica* 69(2), pp. 613–630. doi: 10.1007/s11600-020-00529-7.

Nironen, M. 1997. The Svecofennian Orogen: a tectonic model. *Precambrian Research* 86, pp. 21–44.

Nironen, M. 1999. Structural Evolution of the Loimaa Area, Southwestern Finland. *Bulletin of the Geological Society of Finland* 71(1), pp. 57–71.

Nironen, M. 2017. Guide to the Geological Map of Finland – Bedrock 1:1 000 000. *Geological Survey of Finland, Special Paper* 60, pp. 41–76.

Nordbäck, N. 2024. *Characterisation of Brittle Structures of Bedrock in Southern Finland - Unravelling the evolution and properties of fault and fracture systems and their prediction at different scales Nicklas Nordbäck*. Doctoral Dissertation, University of Turku.

Nordbäck, N., Ovaskainen, N., Markovaara-Koivisto, M., Skyttä, P., Ojala, A., Engström, J. and Nixon, C. 2023. Multiscale mapping and scaling analysis of the censored brittle structural framework within the crystalline bedrock of southern Finland. *Bulletin of the Geological Society of Finland* 95(1), pp. 5–32. doi: 10.17741/bgsf/95.1.001.

Olsson, O., Falk, L., Forslund, O., Lundmark, L. and Sandberg, E. 1992. Borehole Radar Applied to the Characterization of Hydraulically Conductive Fracture Zones in Crystalline Rock. *Geophysical Prospecting* 40(2), pp. 109–142. doi: 10.1111/j.1365-2478.1992.tb00367.x.

Pajunen, M., Airo, M., Elminen, T., Mänttäri, I., and Niemelä, R. 2008. Tectonic evolution of the Svecofennian crust in Southern Finland. *Geological Survey of Finland Special Paper* 47, pp. 15-161.

Piipponen, K., Martinkauppi, A., Korhonen, K., Vallin, S., Arola, T., Bischoff, A. and Leppäharju, N. 2022. The deeper the better? A thermogeological analysis of medium-deep borehole heat exchangers in low-enthalpy crystalline rocks. *Geothermal Energy* 10(1), pp. 1–20. doi: 10.1186/s40517-022-00221-7.

Porsani, J.L., Sauck, W.A. and Júnior, A.O.S. 2006. GPR for mapping fractures and as a guide for the extraction of ornamental granite from a quarry: A case study from southern Brazil. *Journal of Applied Geophysics* 58(3), pp. 177–187. doi: 10.1016/j.jappgeo.2005.05.010.

Romano, V., Bigi, S., Carnevale, F., De'Haven Hyman, J., Karra, S., Valocchi, A., Tartatello, M. And Battaglia, M. 2020. Hydraulic characterization of a fault zone from fracture distribution. *Journal of Structural Geology* 135, pp. 1–14. doi: 10.1016/j.jsg.2020.104036.

Ruuska, E., Skyttä, P., Ahlqvist, K., Nordbäck, N., Barron, P. and Nikkilä, K. 2025. The role of shear zones, faults and the associated fractures on the formation and character of bedrock surface depressions in crystalline bedrock (Turku,

southwestern Finland). *EGUsphere (preprint)*, pp. 1–34. Available at: https://egusphere.copernicus.org/preprints/2025/egusphere-2025-4271/.

Sakaguchi, I. 2017. *Emplacement conditions and wallrock reactions of pegmatitic granitoid dikes, Kopparnäs, SW Finland.* Master's Thesis, University of Helsinki.

Saksa, P., Heikkinen, E. and Lehtimäki, T. 2005. *Geophysical radar method for safeguards application at Olkiluoto spent fuel disposal site in Finland.* 56p.

Sanderson, D.J. and Nixon, C.W. 2015. The use of topology in fracture network characterization. *Journal of Structural Geology* 72, pp. 55–66. doi: 10.1016/j.jsg.2015.01.005.

Serzu, M.H., Kozak, E.T., Lodha, G.S., Everitt, R.A. and Woodcock, D.R. 2004. Use of borehole radar techniques to characterize fractured granitic bedrock at AECL's Underground Research Laboratory. *Journal of Applied Geophysics* 55(1–2), pp. 137–150. doi: 10.1016/j.jappgeo.2003.06.012.

Skyttä, P., Nordbäck, N., Ojala, A., Putkinen, N., Aaltonen, I., Engström, J., Mattila, J. and Ovaskainen, N. 2023. The interplay of bedrock fractures and glacial erosion in defining the present-day land surface topography in mesoscopically isotropic crystalline rocks. *Earth Surface Processes and Landforms* 48(10), pp. 1956–1968. doi: 10.1002/esp.5596.

Skyttä, P., Kinnunen, J., Palmu, J.P. and Korkka-Niemi, K. 2015. Bedrock structures controlling the spatial occurrence and geometry of 1.8Ga younger glacifluvial deposits - Example from First Salpausselkä, southern Finland. *Global and Planetary Change* 135, pp. 66–82. doi: 10.1016/j.gloplacha.2015.10.007.

Skyttä, P. and Mänttäri, I. 2008. Structural setting of late Svecofennian granites and pegmatites in Uusimaa Belt, SW Finland: Age constraints and implications for crustal evolution. *Precambrian Research* 164(1–2), pp. 86–109. doi: 10.1016/j.precamres.2008.04.001.

Skyttä, P., Ovaskainen, N., Nordbäck, N., Engström, J. and Mattila, J. 2021. Fault-induced mechanical anisotropy and its effects on fracture patterns in crystalline rocks. *Journal of Structural Geology* 146, pp. 1–19. doi: 10.1016/j.jsg.2021.104304.

Skyttä, P., Väisänen, M. and Mänttäri, I. 2006. Preservation of Palaeoproterozoic early Svecofennian structures in the Orijärvi area, SW Finland-Evidence for polyphase strain partitioning. *Precambrian Research* 150(3–4), pp. 153–172. doi: 10.1016/j.precamres.2006.07.005.

Smeraglia, L., Mercuri, M., Tavani, S., Pignalosa, A., Kettermann, M., Billi, A. and Carminati, E. 2021. 3D Discrete Fracture Network (DFN) models of damage zone fluid corridors within a reservoir-scale normal fault in carbonates: Multiscale approach using field data and UAV imagery. *Marine and Petroleum Geology* 126, pp. 1–21. doi: 10.1016/j.marpetgeo.2021.104902.

Song, Z., Zheng, J., Zhang, R., Zhu, A., He, T. and Wang, J. 2025. The potential of ground penetrating radar in rock fracture detection: insights from physical model tests and numerical simulations. *Journal of Rock Mechanics and Geotechnical Engineering*, pp. 1–23. doi: 10.1016/j.jrmge.2025.04.036.

Stålfors, T. and Ehlers, C. 2006. Emplacement mechanisms of late-orogenic granites: Structural and geochemical evidence from southern Finland. *International Journal of Earth Sciences* 95(4), pp. 557–568. doi: 10.1007/s00531-005-0049-3.

Tao, M., Chen, X., Cheng, Q. and Binley, A. 2022. Evaluating the joint use of GPR and ERT on mapping shallow subsurface features of karst critical zone in southwest China. *Vadose Zone Journal* 21(1), pp. 1–14. doi: 10.1002/vzj2.20172.

Toivanen, E. 2023. *Zircon and titanite age determinations of felsic and mafic igneous rocks from Orijärvi, southwestern Finland*. Master's Thesis, University of Turku.

Toivanen, E., Vehkamäki, T., Väisänen, M., Kara, J. and O'brien, H. 2025. Geochronology of the felsic rocks in Orijärvi, southern Finland – implications for stratigraphy. *Estonian Journal of Earth Sciences* 74(1), pp. 34–52. doi: 10.3176/earth.2025.03.

Torvela, T. and Ehlers, C. 2010. From ductile to brittle deformation: Structural development and strain distribution along a crustal-scale shear zone in SW Finland. *International Journal of Earth Sciences* 99(5), pp. 1133–1152. doi: 10.1007/s00531-009-0451-3.

Torvela, T. and Kurhila, M. 2022. Timing of syn-orogenic, high-grade transtensional shear zone formation in the West Uusimaa Complex, Finland. *Bulletin of the Geological Society of Finland* 94(1), pp. 5–22. doi: 10.17741/bgsf/94.1.001.

Torvela, T., Mänttäri, I. and Hermansson, T. 2008. Timing of deformation phases within the South Finland shear zone, SW Finland. *Precambrian Research* 160(3–4), pp. 277–298. doi: 10.1016/j.precamres.2007.08.002.

Tsoflias, G.P. and Hoch, A. 2006. Investigating multi-polarization GPR wave transmission through thin layers: Implications for vertical fracture characterization. *Geophysical Research Letters* 33(20), pp. 1–5. doi: 10.1029/2006GL027788.

Vaasjoki, M., Korsman, K. and Koistinen, T. 2005. Overview. In: *The Precambrian Geology of Finland- Key to the Evolution of the Fennoscandian Shield.* Amsterdam: Elsevier B.V., pp. 1–18.

Väisänen, M. and Hölttä, P. 1999. Structural and metamor- phic evolution of the Turku migmatite complex, southwestern Finland. *Bulletin of the Geological Society of Finland* 71(1), pp. 177–218.

Väisänen, M., Mänttäri, I. and Hölttä, P. 2002. Svecofennian magmatic and metamorphic evolution in southwestern Finland as revealed by U-Pb zircon SIMS geochronology. *Precambrian Research* 116, pp. 111–127. Available at: www.elsevier.com/locate/precamres.

Väisanen, M., Mänttäri, I., Kriegsman, L.M. and Hölttä, P. 2000. Tectonic setting of post-collisional magmatism in the Palaeoproterozoic Svecofennian Orogen, SW Finland. *Lithos* 54, pp. 63–81. Available at: www.elsevier.nlrlocaterlithos.

Väisänen, M. and Skyttä, P. 2007. Late svecofennian shear zones in southwestern finland. *GFF* 129(1), pp. 55–64. doi: 10.1080/11035890701291055.

Väisänen, Markku. 2002. Tectonic evolution of the palaeoproterozoic svecoffenian orogen in southwestern Finland. *Annales Universitatis Turkuensis, A II* 154, p. 143.

Walton, G., Lato, M., Anschütz, H., Perras, M.A. and Diederichs, M.S. 2015. Non-invasive detection of fractures, fracture zones, and rock damage in a hard rock excavation - Experience from the Äspö Hard Rock Laboratory in Sweden. *Engineering Geology* 196, pp. 210–221. doi: 10.1016/j.enggeo.2015.07.010.

Wu, P., Johnston, P. and Lambeck, K. 1999. Postglacial rebound and fault instability in Fennoscandia. *Geophys. J. Int* 139, pp. 657–670. Available at: https://academic.oup.com/gji/article/139/3/657/586761.